City Research Online

City St George's, University of London

Citation: Li, Q., Stavropoulos-Vasilakis, E., Koukouvinis, P., Gavaises, M. & Bruecker, C. (2021). Micro-pillar sensor based wall-shear mapping in pulsating flows: In-Situ calibration and measurements in an aortic heart-valve tester. Journal of Fluids and Structures, 105, 103346. doi: 10.1016/j.jfluidstructs.2021.103346

This is the accepted version of the paper.

This version of the publication may differ from the final published version. To cite this item please consult the publisher's version.

Permanent repository link: https://openaccess.city.ac.uk/id/eprint/26351/

Link to published version: https://doi.org/10.1016/j.jfluidstructs.2021.103346

Copyright and Reuse: Copyright and Moral Rights remain with the author(s) and/or copyright holders. Copies of full items can be used for personal research or study, educational, or not-for-profit purposes without prior permission or charge, unless otherwise indicated, provided that the authors, title and full bibliographic details are credited, a hyperlink and/or URL is given for the original metadata page and the content is not changed in any way. For full details of reuse please refer to City Research Online policy.

City Research Online: http://openaccess.city.ac.uk/ publications@citystgeorges.ac.uk

Submitted to Journal of Fluids and Structures

Micro-pillar sensor based wall-shear mapping in pulsating flows: In-situ calibration and measurements in an aortic heart-valve tester

Qianhui Li[1], Evangelos Stavropoulos-Vasilakis, Phoevos Koukouvinis, Manolis Gavaises and Christoph H. Bruecker

School of Mathematics, Computer Science and Engineering, City, University of London, Northampton Square, London, EC1V 0HB, UK

Abstract

Accurate wall-shear stress (WSS) in-vitro measurements within complex geometries such as the human aortic arch under pulsatile flow are still difficult to achieve, meanwhile such data are important for classifying impacts of prosthetic valves on aortic walls. Micro-cantilever beams can serve to sense the WSS in such flows for applications in in-vitro flow tester. However, within pulsatile flows and complex 3D curved geometries such as the aortic arch, the flexible sensor structures are subject to oscillating boundary layer thickness and profile shape, which may not have been taken into account in the calibration procedure. The fluid-structure interaction is sensitive to these changes, thus reflecting also the flow-induced deflection of the sensor tip which is actually the sensing signal. We develop herein a methodology for in-situ calibration of the response of the sensors directly in the complex geometry of the aortic arch, assisted by reference data from numerical simulations of the flow under the same boundary conditions. For this procedure, a quick exchange of the heart valve in the tester with a tubular insert is done to provide a smooth contour in the curved aorta model. Arrays of 500μm long micro-pillar WSS sensors in the aorta model are calibrated under physiological pulsatile flow and used then for mapping the WSS evolution in the arch induced by two different heart valves, showing their difference of impact. The developed methodology completes the in-house built in-vitro flow tester with a reliable WSS measurement technique and provides a unique hydrodynamic testing facility for heart valve prostheses and their impact on the WSS distal along the aortic walls.

Keywords: *wall shear stress, aorta, pulsating flow, micro-pillar sensors, CFD-assisted calibration, heart-valve tester*

1. Introduction

The mean magnitude and fluctuation amplitude of wall shear stress (WSS) in the human circulatory flow system have important influence on possible vascular diseases. For instance, vessel segments exposed to low WSS or oscillating WSS has been reported to be at the highest risk for developing atherosclerosis (Chien et al., 1998; Shaaban and Duerinckx, 2000). Also, oscillating shear forces plus large WSS gradients were linked to the development of intimal hyperplasia (IH) (Haruguchi and Teraoka, 2003) . Direct measurements of the WSS in the vessels are still difficult if not impossible in these complex geometries, therefore most of the data in literature are obtained from detailed velocity field measurements. However, because of limits in spatial and temporal resolution, the results of these measurements show larger variations and suffer from the lack of reliable means for validation against a standard reference (Katritsis et al., 2007). As reported by Potters et al. (Potters et al., 2014), values in the literature for cycle averaged aortic WSS differ over one order of magnitude.

WSS is generally obtained from the wall-normal gradient of the velocity component parallel to the wall. The underlying flow fields could typically be obtained in three ways: (i) in-vivo velocity measurements such as phase-contrast magnetic resonance imaging (PC-MRI) (Markl et al., 2011; Papathanasopoulou et al., 2003; Potters et al., 2014); (ii) in-vitro measurements, e.g. using optical transparent models and Volumetric Particle Image Velocimetry (V-PIV) methods, such as 3D Particle Tracking Velocimetry (3D-PTV), 3D Scanning-PIV or 3D Tomo-PIV (a review of such methods is given in (Raffel et al., 2018b)); (iii) numerical simulations using CFD, see (Gross-Hardt et al., 2018; Lantz et al., 2011; Orlü and Vinuesa, 2020) among many other.

Numerical studies on WSS in biological systems have been proven beneficial for conditions where experimental measurements are inaccessible, whereas it remains partly limited due to uncertainties in the boundary conditions, the extraction of the exact geometry of the blood vessels as well as the mesh sensitivity (Gross-Hardt et al., 2018); accurate calculation of the velocity gradients at the wall requires a high-resolution mesh at the near-wall region, which results to high computational cost. A typical Reynolds number in the aorta is of the order of 10,000; this requires high-performance computing power to achieve sufficient resolution down to the order of the Kolmogorov length scales, typically tens of microns in such flows. Such resolution is even necessary for laminar flows in regions, where the flow locally exhibits sharp velocity gradients in geometries like bends, bifurcations, junctions and separation zones.

[1] Corresponding author: Email address: Qianhui.Li@city.ac.uk

In general, in-vivo flow mapping using four-dimensional flow Magnetic Resonance Imaging (4D MRI) can achieve a typical spatial resolution of 1.5-2.5 mm, a temporal resolution of 30-60 ms and slice thickness of 5-8 mm (Stankovic et al., 2014). Higher resolution of the measured velocity profiles can only be achieved in relatively straight vessels (Katritsis et al., 2007). Another equally important factor is the accuracy in detecting the wall position relative to the velocity field, which remains a challenging task in 4D MRI (Zimmermann et al., 2018). There are only a few reports on the reproducibility and reliability of WSS estimation obtained from 4D MRI measurement (Markl et al., 2011). A combined study of 4D MRI measurement and CFD predictions on WSS in a laminar flow through a carotid bifurcation model has been reported in (Papathanasopoulou et al., 2003), concluding that the 4D MRI measurement was not able to detect the high WSS values along the inner walls of the bifurcation compared to the values predicted by the numerical simulation. As for the in-vitro measurement, V-PIV measurements suffer the same resolution problems. In addition, detecting the wall position is a non-trivial part. Kunze et al. (Kunze et al., 2008) first highlighted the importance of accurate wall-position information in 3D-PTV for accurate WSS measurements. To overcome the problem with the actual wall-position, they developed mirror-image 3D-PTV, where the original particle image and its mirror image reflected from the wall are used as additional inputs into the tracking data. Their results of a transitional wall-jet showed an excellent agreement between the calculated WSS and the theoretical values. In more complex geometries, 3D-PTV often requires utilization of larger particles of the order of 100 µm in order to improve light-efficiency for sufficient exposure in the required high-speed recordings. In (Gülan and Holzner, 2018), particles with a diameter of 200 µm have been used for 3D-PTV flow studies in the aortic arch. In contrast, a light-sheet-based PIV application can use micron-size tracer particles and therefore can achieve two orders of magnitude higher spatial resolution. This method has become a standard flow diagnostic technique for in-vitro studies (Raghav et al., 2018). However, it provides only the 2D in-plane velocity field and requires a much higher seeding density, which is sometimes difficult to achieve near the wall.

A novel tracer-less WSS measurement method with high potential for in-vitro applications in biological flows was introduced recently in (Bruecker et al., 2005); this is based on a high-resolution recording of the tip motion of wall-mounted flexible micro-pillar sensors, acting similar to micro-cantilever beams subjected to flow-induced drag forces. This method has recently been adapted to WSS measurements in aortic flows; results for different heart valve prostheses with 1 mm length micro-pillar sensors were reported in (Li et al., 2020), not without mentioning remaining limitations of these sensors regarding the spatial and temporal resolution and possible measurement uncertainties introduced by the sensor calibration procedure. To achieve an accurate measurement of the WSS with this technique, it is of great importance to calibrate the sensors in an appropriate way and under similar flow conditions as in the actual experiment (Bruecker et al., 2007). Ex-situ calibration might be not reliable for such applications as reported herein as it is hard to achieve the same working conditions in terms of flushness of wall-mounting of the elastic cantilevers, their clamping, the underlying flow conditions, possible changes of the elastomeric material parameters with time in the liquid or with temperature, to name only a few reasons.

In the present paper the sensors are calibrated in-situ with a single systolic flow pulse (the calibration pulse) and using reference data from complementary flow simulations at the same boundary conditions. For this procedure the aortic valve is exchanged with a thin tubular insert, which transforms the aorta phantom into a tubular bend with constant cross-section (180° curved bend). For the phase of flow acceleration in the calibration pulse the flow remains laminar and homogeneous, which is used for calibrating the static and dynamic response of the sensors with input from the simulated velocity profiles in the boundary layer at the locations of the sensors. After the calibration, the tubular insert is exchanged with the actual mechanical heart valve (MHV) under investigation and the sensors are used to map the wall-shear (WS) evolution along the aortic wall distal to the valve under physiological flow conditions. It is the first time that such a CFD-assisted verification of the sensor response is possible at the same pulsatile flow conditions and geometrical conditions as in the actual experiment with MHVs. The present study goes further on addressing the issue of uncertainty in WSS measurements within such complex geometries as reviewed above. A recent study published during the review phase also hints on the lack of a systematic comparison between experimental and numerical values of the WSS for realistic aortic flow conditions (see (Corso et al., 2021)). The herein described methodology is new and completes the in-house built in-vitro flow tester with a reliable WSS measurement technique and provides a unique research facility for future hydrodynamic testing of heart valve prostheses with focus on WSS diagnostics. The methods are described in the following Section 2 and the results are given in Section 3, which is followed by discussions and conclusions.

2. Materials and Methods

2.1 Experimental study

2.1.1 Heart valve tester

Figure 1a shows a principle sketch of the aortic flow duplicator (heart valve tester) with the transparent model of the human aorta placed at the bottom of a liquid-filled transparent container (see also Figure 1b for the sketch of top view and Figure 1d for the actual frontal view of the experimental set up), with a smooth converging inlet nozzle with initial diameter D_N=40mm and length of $2D_N$. The flow through the model is generated with a programmable pulse generator as described in our previous study (Li et al., 2020). A 58%/42% by mass glycerine-water solution is used as working liquid having a density ρ_f = 1140 kg·m^{-3} and dynamic viscosity μ= 5 mPa·s at 38°C. Therefore the fluid is considered as Newtonian, with constant kinematic viscosity of $\nu = \mu/\rho = 4.386 \cdot 10^{-6}\, m^2/s$, and the aorta walls as rigid. Note that heart valve testers usually work with Newtonian liquids, first as the vessel diameter of the aorta is large and non-Newtonian effects can be neglected therein (see (Fung, 2013; Kim et al., 2004)) and secondly to ensure standardized working conditions between different testers when used for FDA regulation and approval. The air cushion above the liquid level is used to model systemic vascular compliance. The imposed flow profile is given in Figure 1c, which resembles a physiological systolic flow pulse with the maximum velocity reached at about 30% of the cycle, giving a peak Reynolds number of about 5400 (see section 2.1.2). The aorta phantom is fabricated from transparent Perspex and has the form of a regular 180-degree bend with a constant inner diameter (D_A=25 mm), curved along the plane of symmetry (see Figure 2).

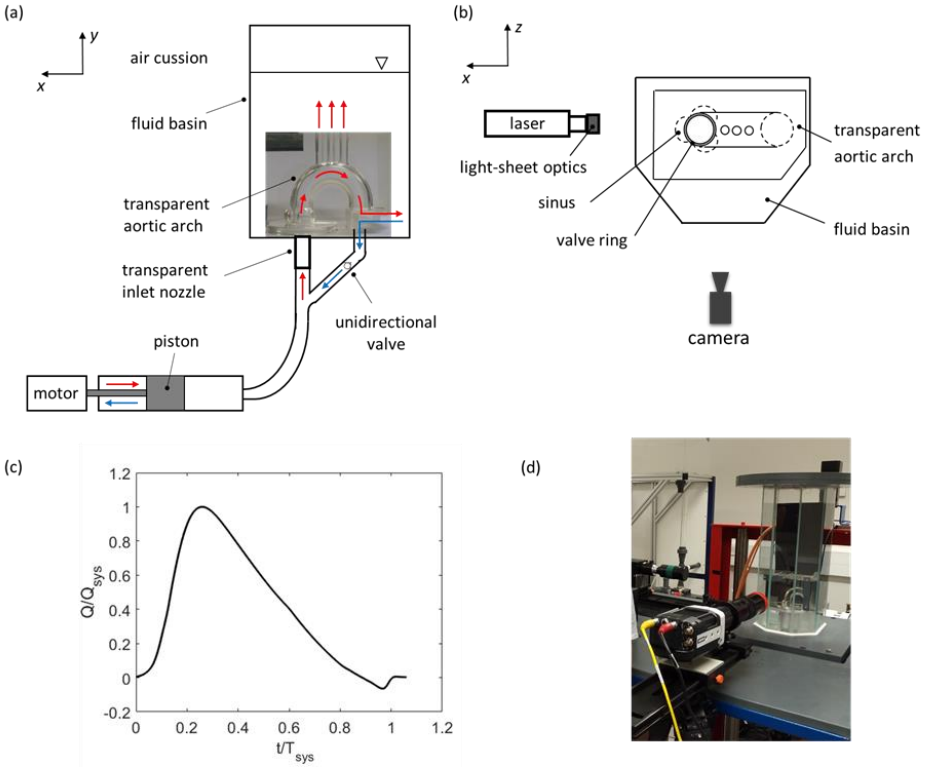

Figure 1. (a) Sketch of the pulse duplicator. (b) Top view of the experimental setup. (c) Inlet flow condition over the systolic cycle, where Q_{sys} is the peak flow rate and T_{sys} =386 ms is the systolic time (d) Frontal view of the setup.

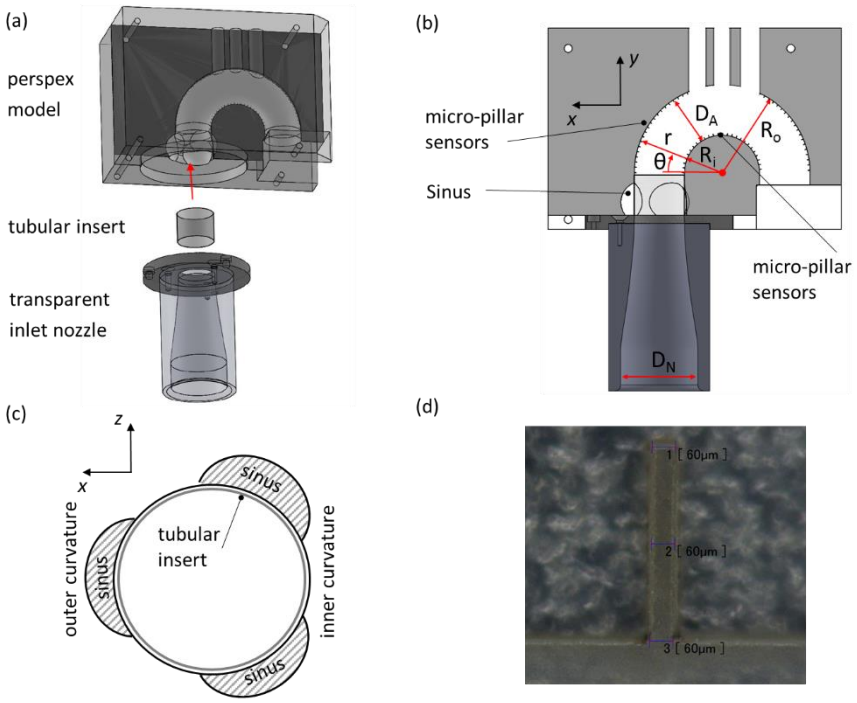

Figure 2. (a) Aorta model with removable tubular insert in the valve plane (b) Frontal view of the sensor placement in the symmetry plane of the aorta model (diameter of the inlet nozzle D_N=40mm, diameter of the aorta D_A=25 mm, radius of the inner curvature R_i=18 mm, radius of outer curvature R_o=43 mm). (c) Cross-section in the valve plane. (d) Microscopic image of a single micro-pillar sensor.

Furthermore, there are three symmetric sinuses of Valsalva (SOV) at the aortic root and arterial branches at the top of the bend. The geometrical parameters of this model are the same as the silicone model used in (Li et al., 2020). The Perspex model is fabricated from two symmetric halves clamped together, sealed at the centre plane with a thin elastic silicone sheet (Wacker ELASTOSIL Film 2030 Wacker Chemie AG, Munich, Germany. Film thickness 200 µm, post-curing density: ρ_S=1500 kg·m^{-3}, Shore A: 27, elastic modulus E= 1.34 MPa). The circular edge of the sheet is micro-structured such that it contains a row of radially outgoing extensions of rectangular flexible cantilever beams, i.e. the micro-pillar sensors. The dimensions of the micro-pillar are as follows: beam length L = 500 µm, beam thickness h=60 µm, beam width b=200 µm. The microscopic structure of the micro-pillar shown in Figure 2d was measured by a digital microscope (VHX-700F, KEYENCE Ltd, UK) equipped with a VH-Z20R lens. The inner part of the edge follows the extrados of the aorta and is flush to the wall such that the root of the sensors is clamped between both halves of the model. The angular location of these micro-pillars starts from θ=0˚ with an angular interval of 7˚ at the inner wall and 3.5 ˚ at the outer wall.

In the calibration procedure, a thin-walled tubular insert (outer and inner diameters of 25 and 24.6 mm, respectively) is placed in the arch at the same location where typically the aortic valve is located. When the systolic flow pulse is generated, the bulk flow smoothly enters through the step-free inlet into the tubular bend. WS measurements in this flow pulse are compared to the reference data of the CFD simulations (see section 2.2 and Appendix B) to verify the calibration. Thereafter, the tubular insert is removed and the actual MHV prosthesis is inserted at the entrance of the aorta. The same systolic flow pulse is then applied again to investigate the WS at the aortic walls distal of the valves. The different types of MHVs are the same as used in (Li et al., 2020) and are displayed in Figure 3 in open and closed situation, including the St. Jude Medical Regent bileaflet mechanical heart valve (SJM Regent valve) (St. Jude Medical Inc., Minnesota, U.S.) and the Lapeyre-Triflo FURTIVA trileflet mechanical heart valve (Triflo valve) (Novostia SA, Neuchâtel, Switzerland).

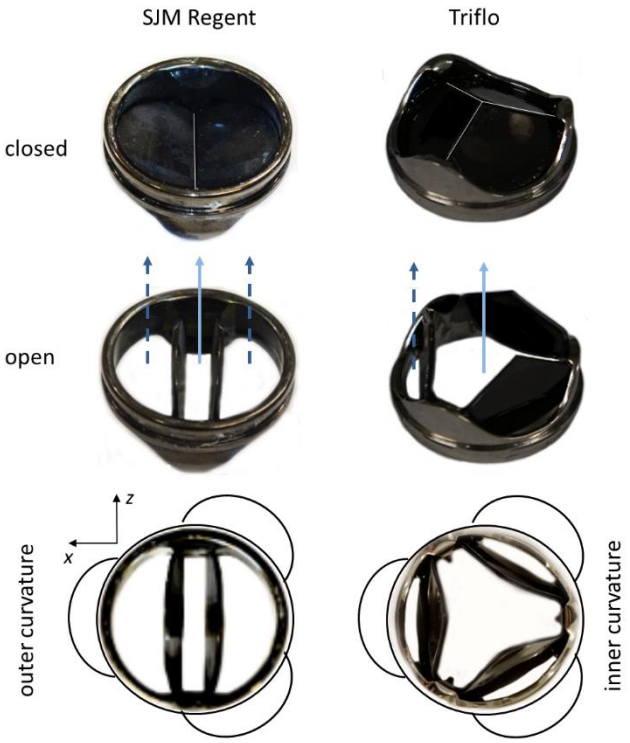

Figure 3. SJM Regent valve: one leaflet is facing the left sinus at the outer curvature of the aorta while the other leaflet is in the middle between two sinuses, facing the inner curvature. Triflo valve: the axes of the leaflets face the sinuses in all three directions.

2.1.2 Flow measurements using High-Speed Particle Image Velocimetry (HS-PIV)

Complementary flow field measurements have been also obtained using High-Speed Particle Image Velocimetry (HS-PIV) in the silicone model, as presented in (Li et al., 2020) ; as already mentioned, this has the same geometry as the Perspex model but offers better optical quality in regions deep inside the arch. The arrangement of the experimental setup is shown in Figure 1b. A continuous wave Argon-Ion laser (Raypower 5000, 5W power at λ=532 nm, Dantec Dynamics) is used as an illumination source. The output laser beam is approximately 1.5mm in diameter and is further expanded into a sheet, illuminating the symmetry plane of the aorta. Small tracer particles (fluospheres, Dantec Dynamics, mean diameter 30 μm, and density $\rho_p = 1040\ kg \cdot m^{-3}$) are added to the working liquid. For all recordings, a high-speed camera (Phantom Miro 310, Ametek) equipped with a lens (Tokima Macro f=100 mm, F 2.8) is used.

PIV measurements with three different fields of view are performed, including a full field PIV measurement for the global flow field of the ascending aorta (AAo), zoom-in PIV measurement covering the diameter of the aorta (D_A corresponds to a scale of 688 pixels on the image sensor) to measure the axial velocity profile along cross-section e.g. θ=21˚, as well as micro-PIV measurement for capturing the near wall flow field. The measurement configurations are listed in Table 1. An in-house developed MATLAB code is used to post-process the flow field recordings, which contains the image pre-processing and 2D cross-correlation of successive images to calculate the particle displacements with subpixel accuracy using a Gaussian fit of the correlation peak in the correlation plane, a standard method in Digital Particle Image Velocimetry (DPIV) (see (Raffel et al., 2018a)). The data processing process has also been described by the authors' in (Li and Bruecker, 2018). Processing is done in small interrogation windows with an iterative grid refinement method. The configurations of the final window size and the overlap ratio are also given in Table 1.

Table 1. Configurations of optical measurements and data processing.

Region of interest	Frame rate (fps)	Resolution (px^2)	Field of view (mm^2)	Interrogation window (px^2)	Overlap ratio (%)
Full-field PIV	5400	576 × 768	57.6 × 76.8	32 × 32	50
Zoom-in PIV	5400	576 × 768	20.9 × 27.9	128 x 16	50
Micro-PIV	7200	576 × 768	7.6 x 10.2	190 × 48	75
Micro-pillar	2000	1280×800	8.5×5.3	32 × 24	75

The peak inlet velocity observed in the plane of the circular entrance into the bend reaches a value of U_p = 0.95 m·s^{-1}. The Reynolds number, defined with the peak velocity, is $Re = \frac{\rho U_P D_A}{\mu} = 5415$. This indicates a turbulent flow in the peak flow situation. However, in pulsatile flows, the transition to turbulence also depends on the Womersley number (α) and the pulsation amplitude (A) (Stettler and Hussain, 1986; Trip et al., 2012). These parameter in the present study are $\alpha = \frac{D_A}{2}\sqrt{\frac{\omega\rho}{\mu}} = 16$ and $A = U_p/U_m = 5$, where ω is the driving frequency. A variety of studies (Stettler and Hussain, 1986; Xu et al., 2017) on pulsating pipe flows for Womersley numbers $\alpha > 10$ have reported that the transition in such cases is further delayed into the deceleration phase. This agrees with our observations as shown by the flow visualization picture in Figure 9 taken at the peak systole time, which demonstrates a laminar and homogeneous flow in this flow channel. In the following, laminar flow is used for the calibration of the WSS sensors.

2.1.3 Micro-pillar sensor methodology

Micro-pillar WSS measurements follow the principle of measuring the bending of a one-sided clamped microscopic cantilever beam, situated in the boundary layer and actuated by the drag forces from the flow around the pillar; the measurement principle and methodology is given in detail in (Bruecker et al., 2007; Bruecker et al., 2005). Theoretically, when the length of the pillar is small enough such that it is fully submerged in the viscous sublayer of the near-wall flow boundary layer, the flow-induced bending moment *M* is proportional to the WSS, which can be measured by the tip displacement of the micro-pillar relative to its position at fluid rest. As shown in our previous work (Bruecker et al., 2007; Bruecker et al., 2005), the dynamic response of such a micro-pillar sensor in liquids follows closely that of a 2nd order harmonic oscillator in overdamped situation (quality factor $Q < 1/\sqrt{2}$), which is described by a nearly constant gain until the cut-off frequency f_C, where the gain rolls off. The amplitude and phase response of such an oscillator are given by (Van Eysden and Sader, 2006):

$$|H(j\omega)| = \frac{1}{\sqrt{\left(1-\frac{\omega^2}{\omega_n^2}\right)+\frac{1}{Q^2}\frac{\omega^2}{\omega_n^2}}} \quad , \quad \varphi(j\omega) = -arctan\left(\frac{1}{Q}\frac{\omega\cdot\omega_n}{\omega_n^2-\omega^2}\right) \tag{1}$$

with the flexural natural frequency ω_n in the liquid environment. For a rectangular cantilever beam ω_n is related to the natural frequency $\omega_{n,vac}$ in vacuum as follows (see (Van Eysden and Sader, 2006)) :

$$\omega_n = \omega_{n,vac}\left(1+\frac{\pi\rho_f b}{4\rho_S h}\right)^{-1/2} \quad , \quad \omega_{n,vac} = \frac{1.875^2}{L^2}\sqrt{\frac{EI}{bh\rho_S}}, \tag{2}$$

where *E* is the Young's modulus and *I* the moment of inertia of the beam cross-section, which is $I=bh^3$ / 12 for a rectangular beam. With the given data, the expected resonance frequency (flexural) for the sensor in the liquid used herein is estimated to be ω_n = 4210 rad/s, which takes into account the added mass effect of the viscous liquid surrounding the sensor. From that we can estimate the measurement range, defined as the range of nearly constant gain (and small phase shift) below the cut-off frequency $fc=0.3\ \omega_n$. This theoretical estimation will be verified later by experimentally determined values of the gain, cut-off frequency and quality factor *Q* from the herein described CFD-assisted calibration of the sensor response.

Of further importance to characterize the sensor properties is the sensitivity *S*. According to (Bruecker et al., 2005), the sensitivity could be defined as the ratio of the pillar tip deflection amplitude Q_S to the wall shear stress. As the pillar tip's deflection is proportional to the flow-induced bending moment *M*, we use herein the definition of the sensitivity as $S = M/\gamma$, where γ is the wall shear rate. Theoretically, for very small pillars, the sensitivity should remain constant which is then determined ideally within a defined shear flow, e.g. a specially adapted cone-plate type viscometer as shown in (Bruecker et al., 2005). However, the flow condition we are investigating herein is a pulsating flow with a developing boundary layer with time-varying velocity profiles. Therefore, further analysis is required to understand the effect of velocity profile shape, boundary layer thickness and velocity magnitude on the sensitivity. This is done herein for the micro-cantilever beams in analogy to the derivations made for slender wind-hairs in the work from Dickinson (Dickinson, 2010). The pillar is considered as a one-sided clamped cantilever beam (linear-elastic Euler-Bernoulli beam theory) with maximum deflection less than 10% of the pillar length. Furthermore, the bending moment acting on the beam is determined from the quasi-steady flow approximation of the local drag. The calculation of the resultant moment at the base of the pillar is as follows (Dickinson, 2010)

$$M(t) = \int_0^L g(t,\xi)\xi d\xi, \tag{3}$$

where $g(t,\xi)$ is the instantaneous load intensity that acts normal to the longitudinal axis with units of force per unit length at any longitudinal location ξ. $g(t,\xi)$ could be estimated as

$$g(t,\xi) = \frac{1}{2}C_d\left(Re_\xi\right)\rho_f b u(t,\xi)^2, \tag{4}$$

where ρ_f is the fluid density, *b* is the width of the beam, *u* is the flow velocity incident on the longitudinal axis of the pillar and C_d is the drag coefficient. C_d is determined as a function of the local Reynolds number. It has been reported that at low *Re* (*Re*<10^2) different shape of the cross section shows a similar relationship of drag coefficient with the *Re (Prandtl, 1952; Yuce and Kareem, 2016)*. We herein use the same relationship as introduced by Dickinson (Dickinson et al., 2012; Dickinson, 2010) which uses a least-squares fit to empirical data ((Prandtl, 1952), p.190) for the drag coefficients of long circular cylinders in cross-flow at $Re_\xi = 10^{-1}, 10^{-0}$ and 10^1 with the R-squared value of 0.996, leading to the following linear logarithmic expression:

$$\log C_d = -\frac{2}{3}\log Re_\xi + \frac{5}{2}, \tag{5}$$

where $Re_\xi = \frac{u(t,\xi)b}{\nu}$. According to (Dickinson et al., 2012), Eq. (5) assumes an infinite cylinder in cross-flow and the end effect of the finite length of pillar is not accounted. Previous study by Jana et al. (Jana et al., 2007) has shown that C_d varies by less then 5% for cantilevers with 10:1 and 200:1 aspect ratio in steady flow when 1< $Re_\xi < 63$ which covers the Re_ξ of the present study, indicating that end effects are small.

Substituting the load intensity Eq. (4) into the resultant moment Eq. (3), it yields

$$M(t) = \int_0^L \frac{1}{2}C_d\left(Re_\xi\right)\rho b u(t,\xi)^2 \xi d\xi \tag{6}$$

Later in section 3.2 in the paper we use Eq. (5) and (6) to determine the sensitivity of the sensor with data from the local velocity profiles around the sensors, which are obtained from the CFD.

2.1.4 Digital image processing of the sensor tip displacement

The tip bending of the sensors at the symmetry plane of the Perspex model of the aortic arch is recorded with a digital camera for all sensors simultaneously and transferred via image processing into a tip displacement vector, which is tangential to the wall. The high-speed camera used is the Phantom Miro 310 Ametek, equipped with an inverted telescopic lens (Model K2/SC™, Infinity Photo-Optical Company, Boulder, CO); a resolution of 1280×800 pixels, recording at 2000 fps was utilized. These settings are listed also in Table 1. It provides a field of view of 8.5×5.3 mm^2 as shown in Figure 5a, and captures the motion of an array of 11 micro-pillars located at the inner curvature simultaneously with a resolution of 150 pixels/mm. To improve the contrast in the images, the tips of the sensors are fluorescent-labelled by fluorescent micro-spheres (PMMA-RhB-Frak-Paticles, Dantec Dynamics, peak emission at 584 nm, peak absorption at 540 nm), which have maximum absorption near the wavelength of the illuminating laser light. A long pass filter (transmission wavelength: 560 - 1650 nm, Edmund Optics Ltd) was applied to block all light from the laser and reflections from the aorta model, and thus, only transmitting the light of the fluorescent-labelled tips. Thus, the tips of the micro-pillar appear as bright dots against a black background. Additional fluorescent markers at the inner wall of one half of the aorta model provide data on a possible motion of the model during the flow pulse. The processing steps of the measurement chain are listed as follows: a) detect vibrational model motion by marker processing, b) subtract vibrational model motion by image transformation, c) dewarp images such that the circular

arcs along the polars of constant pillar height unfolds into a linear unwrapped image segment, d) process the tip displacement between the unfolded images at rest and in the flow pulse, e) postprocess the data. In this section the data are presented in pixels units to present the tip displacement values in relation to the pixel resolution of the camera (for conversion to physical displacement in mm use the optical conversion factor 1 mm= 150 px).

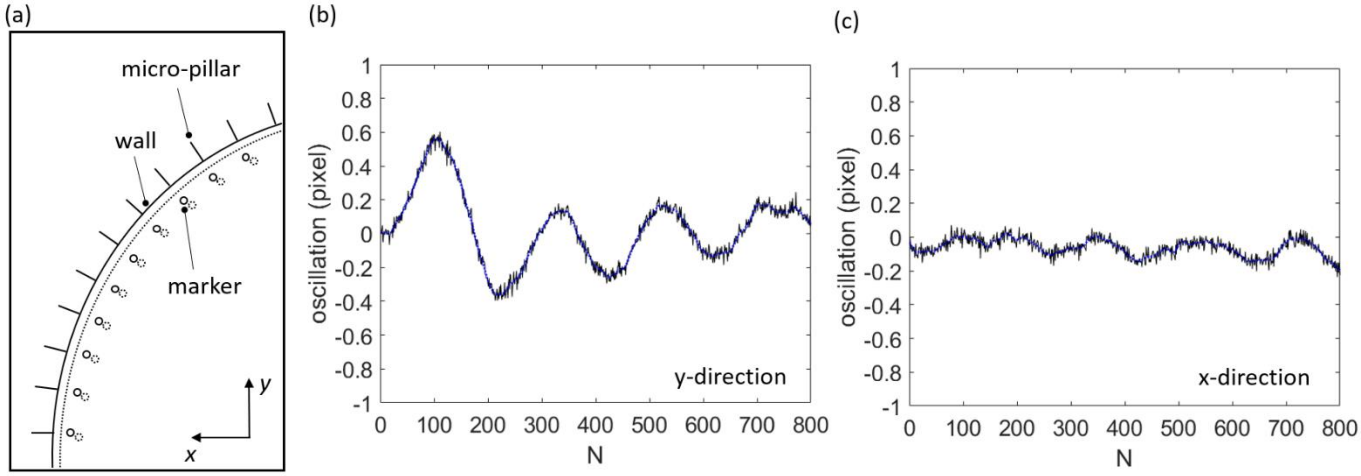

Figure 4. Correcting for vibrational motion of the whole aorta model. (a) capturing the vibrations in the images during the flow pulse (*N* = index of the image number in the sequence) by processing the marker positions and comparing those to the position at rest via 2D cross-correlation. Illustration of shift of the model seen by the dislocated positions (dashed marker) relative to the marker to the situation at fluid rest (solid markers). (b) and (c) typical profiles of vertical and horizontal motion of the model during the flow pulse.

Figure 4 shows a typical vibrational motion of the model during the flow pulse, which was obtained by tracking markers on the inner side of the model using a 2D cross-correlation procedure similar as in DPIV (Raffel et al., 2018a). In the next step, those data are used to preprocess the image sequence such that the vibrational motion of the aorta model in the flow pulse is corrected to zero in the complete image sequence from begin to the end of the flow pulse (the marker position then exactly overlap in the whole sequence). This is done via a 2D linear image translation (bi-linear interpolation) to correct the relative motion. In the next step, another image interpolation is done to unfold the polar arrangement of the pillars presented in Figure 5a such that they appear relocated along a straight line with the tangential displacement of the pillar's tip now converted to the horizontal direction as shown in Figure 5b. Finally a 2D cross-correlation processing similar as in DPIV (see (Raffel et al., 2018a)) is used to detect the pillar tip motion (comparing flow-off with flow-on situation) in small interrogation windows located at the centre of the pillar tips of 32 × 24 px^2; see the zoom-in view of the interrogation window in Figure 5b. Again, subpixel resolution is achieved by fitting the correlation peak similar as in DPIV.

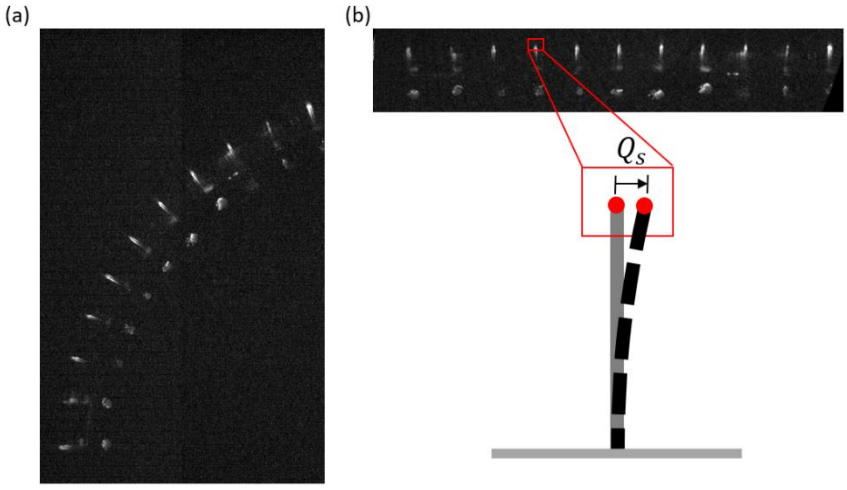

Figure 5. (a) Original image showing the polar arrangement of the micro-pillar WSS sensors at the inner curvature of the aortic arch and (b) after unfolding the polar coordinates into a horizontal coordinate by dewarping the image (a).

A subset of enlarged windows shows the typical windows of the pillar tip (at the situation of no-flow and flow with a displacement of pillar's tip Q_S, which are used for the 2D cross-correlation procedure (note that the relative shift is only about 2 px in the images).

The tip displacement from the measurements can be resolved down to a resolution of 0.4 µm (minimum resolution in pixel = 0.06 px). This limiting value calculates from the error-propagation of the standard error of all digital image processing steps including vibrational motion correction, image dewarping and tip displacement detection using 2D cross-correlation. The combined standard error is calculated as σ_c= 0.06 px, which corresponds to a physical scale of 0.4 µm, hence defining the resolution limit. Note, that a camera with higher pixel resolution than the one used herein can provide higher accuracy, proportional to the increase in pixel resolution.

2.1.5 Data post-processing

The signal processing chain of the tip displacement data is illustrated in Figure 6 exemplary for the tip displacement of the pillar at θ=21˚ over the full number of images in the recorded sequence of the calibration pulse (*N* = index of number of image in the sequence, conversion in time is by $N_{systole}/T_{sys}$ = 772/386 ms where $N_{systole}$ is the total image number of the systolic cycle). Again, the data are presented in pixels units over image number to present the raw data in relation to the pixel resolution and high-speed frame-rate of the camera. The profile indicates a maximum value of the tip displacement of about 2 px, corresponding to 13.3 μm (minimum resolution 0.4 µm) which is 2.66% of the length of the micro-pillar. Because of such small bending the pillar tips remain nearly at the same wall-normal distance in the images (Bruecker et al., 2007). A Fourier series curve fitting procedure (The MathWorks) has been applied (series of 7 sine curves) to remove high-frequency oscillations from the data. Because of the open endings of the model, the flow experiences an impedance jump which causes part of the flow pulse to be reflected back (known as artificial dicrotic notch in pulse-duplicators, see (Politi et al., 2016)). This reflection overlaps with the original flow pulse signal and causes a small oscillation in the sensor signal during flow deceleration at the late phase of the systolic pulse. The outlet boundary conditions within the CFD simulations prevent such a reflection, hence for a direct comparison of the experiments with the CFD data it is required to remove this artificial oscillation from the signal. Test with different band-pass filter finally showed, that the overlaying oscillation due to the dicrotic notch can be approximated mathematically with the profile of a sine-Gaussian pulse:

$$f(N) = A \cdot \sin\left(\frac{2\pi N}{\lambda} + \varphi\right) \cdot e^{-\frac{1}{2}\left(\frac{N-\mu}{\sigma}\right)^2}. \quad (7)$$

The coefficients best fitting the artificial dicrotic notch were determined as follows: magnitude *A* = 0.23 px, wavelength λ = 160 images (corresponding frequency 12.5Hz), phase shift $\varphi = \frac{2\pi}{\lambda} \cdot 411$ images, center posititon of the pulse at image number $N = 381$ and standard deviation σ= 100 images. This form of the reflection pulse is seen on all sensors at the same time and was removed from the original signal by subtracting Eq. (7) before the curve fitting is applied (Fourier series, 7 sine curves). This is the final data set of the pillar tip bending, which has removed all fluctuations above frequencies of 150 Hz, which are considered as non-coherent and random in the range of investigated flow conditions.

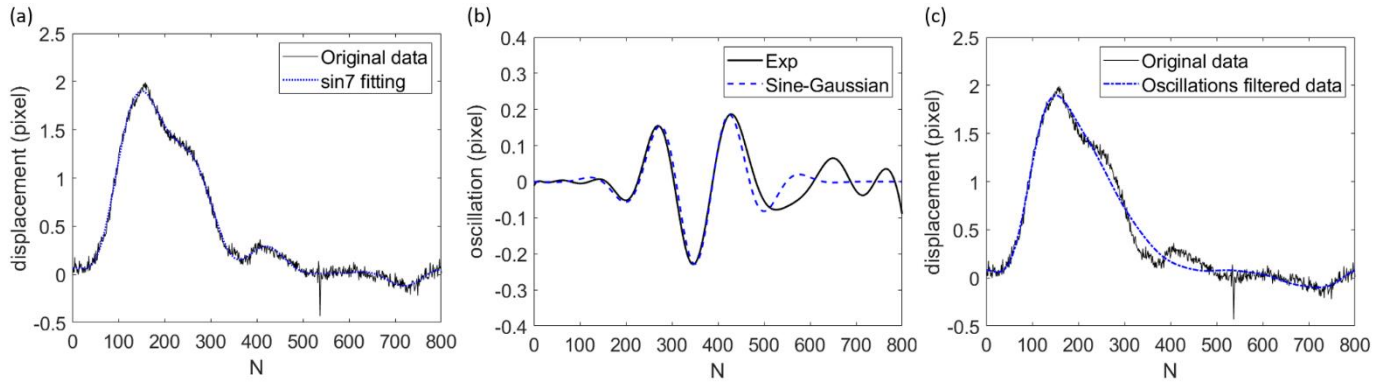

Figure 6. (a) Plot of the measured sensor signal in the calibration pulse, shown by the black line and overlaid with a Fourier series fitting denoted by the blue dot line. (b) Small-amplitude oscillation of the tip displacement induced by the pressure pulse reflection at the open endings of the aorta model (artificial dicrotic notch) and fit with a Gaussian-modulated sinusoidal curve. (c) Tip displacement after removal of the artificial dicrotic notch effect.

2.2 Numerical simulations

2.2.1 Set up of the computational domain

Numerical simulations of the flow are performed using OpenFOAM (Weller et al., 1998). The flow simulations are carried out on an aorta model, identical to the geometry used in the calibration experiments, with the tubular insert covering the sinus region. Identical to the experiments, the fluid is considered as Newtonian, with constant kinematic viscosity of $\nu = \mu/\rho = 4.386 \cdot 10^{-6}\, m^2/s$, and the aorta walls as rigid. The reason for that simplification is the purpose of the CFD study to support the calibration of the sensors used in the heart valve tester (see Appendix B for a detailed discussion of the rheology of blood). Cylindrical flow compartments are added at the outlets of the aorta and the arterial branches to facilitate open-end boundary condition as in the experiments, as shown in Figure 7. At the inlet, the time dependent volumetric flow rate, measured during experiments, is assigned as boundary condition and a uniform block velocity profile along the diameter is imposed. The upstream extension of the inlet nozzle is chosen $4D_N$ long so that the flow would be developed before the converging part; the length of the extension is determined by numerical tests of the same pulsatile flow on a long straight tube. On the outlet volumes, zero-gradient velocity and fixed total pressure boundary conditions have been assigned, replicating the experimental conditions. The total pressure is set equal to ambient atmospheric pressure (1bar) and thus the static pressure to be imposed is calculated using the local velocity value. Standard no-slip velocity boundary conditions are imposed on the aorta walls.

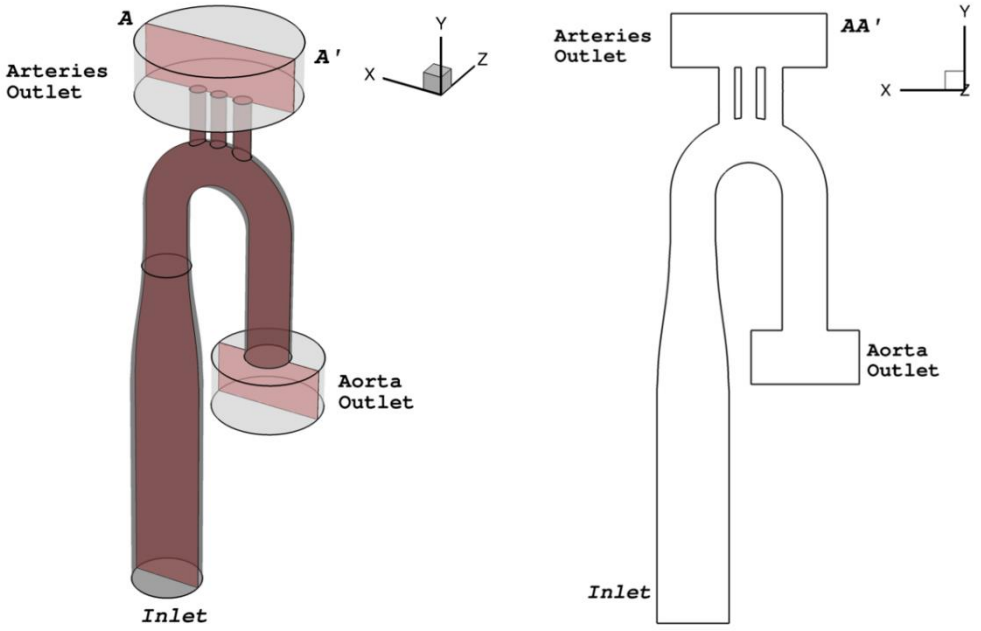

Figure 7. The computational domain of the aorta model. The inlet has a total length of $6D_N$ ($4D_N$ before the convergent part). Two volumes have been put at the outlet of the aorta and the outlet of the arterial branches. The plane AA' corresponds to the side centre plane. The nozzle has a diameter of D_N=40mm.

For pulsatile vascular flows different meshing approaches can been used, as described in (Tu et al., 2015). In the current numerical study, because the domain consists of the aorta, as well as three arterial branches, an unstructured tetrahedral mesh is used. The choice of the tetrahedral mesh is based on its automatic, fast and straightforward generation process.

The walls and the boundaries of the computational domain are triangulated, then structured layers are inserted over the walls to better resolve the boundary layer and finally the volume is discretised by unstructured tetrahedral cells. The aortic arch is discretised by 248 cells on the circumference and 130 along the inner and 300 outer arch, resulting in a triangular mesh of characteristic size between $D_A/80$ and $D_A/57$. In addition, 10 cell layers over the walls are added, with growth ratio 1.2 and first cell size $y_1 = 0.0396\, mm$, which adheres to the condition of $y_+ \leq 1$ that, considering the peak velocity Reynolds number, sets as a limit the value $y_1^* = 0.0594\, mm$. The sum of the 10 layers

covers the total height of an estimated boundary layer thickness of 1mm, the first cell's height corresponds to the 0.4% of the boundary layer and the last cell's height to the 20.5%. The layers are constructed by inflation of the boundary triangular cells, thus forming structured prism cells next the wall. The core volume of the mesh is composed by homogeneous tetrahedra with characteristic size $D_A/100$ in the aortic arch. The grid coarsens towards the inlet and outlets. This results in a 9 million cell mesh. A thorough description of the computational mesh along with a grid independence study and a discussion about the spatial resolution are presented in Appendix B. Three meshes have been tested and the one described hereabove is the medium mesh, referred as middle; results presented hereafter refer to this middle mesh.

2.2.2 The computational algorithm

The PIMPLE algorithm (Moukalled et al., 2016) was used to solve numerically the incompressible Navier-Stokes equations

$$\nabla\vec{u} = 0, \tag{8a}$$

$$\frac{\partial\vec{u}}{\partial t} + \nabla\vec{u}\vec{u} = -\nabla\frac{p}{\rho} + \nabla\nu(\nabla\vec{u} + (\nabla\vec{u})^T), \tag{8b}$$

In the simulations performed, the stress term (second on the right-hand side of Eq. (8b)) is calculated and not modelled. The transient nature of the pulsatile flow under consideration characterized by a high Womersley number, along with the moderate Reynolds number of the flow, suggests that turbulence is not developing throughout the first part of the systolic cycle until peak flow. Rather, turbulence is expected to play an increasingly important role during the deceleration phase (after peak systole) where flow separation develops and transition initiates, see also (Stettler and Hussain, 1986; Trip et al., 2012) (See Appendix B for more details).

An implicit Crank-Nicolson scheme is chosen for the time integration and a second-order central differencing scheme is used for the spatial discretisation. The time step is automatically adjusted in order for the maximum calculated Courant number to always respect Courant-Friedrichs-Lewy (CFL) condition $Co_{max} = \Delta t \frac{1}{2V}\sum_{faces}|\phi_i| \leq 1$, with regards to the magnitude of the fluxes ϕ_i on the faces of the computational cells. Additionally, the maximum time-step is restricted to 0.1 ms, in order to ensure that all the structures of the flow are resolved.

3. Results

From the simulations, velocity data are extracted along the diameter of the aorta on the locations of the micro-pillars and the WS is calculated. Except otherwise stated, the numerical results reported in the following paragraphs correspond to the side view central plane *AA'*, annotated in Figure 7, where also the array of micro-pillars is placed. The micro-pillar located at θ=21˚ cross-section has been selected to present the experimental results, to compare with the numerical predictions and to be used for the calibration of the measurement apparatus.

3.1 Global flow field and boundary-layer

In Figure 8(a), the axial velocity profile as calculated by the CFD simulation is plotted, on four different instances along the pulse. The development of the boundary layer over the walls of the aorta and the absence of recirculation in the specific position, are clearly shown. The boundary layer is continuously growing in the flow pulse from zero at rest to about 1 mm at the early ramp (t/T_{sys} = 0.14) and finally to a thickness of about 1.5 mm at the peak (t/T_{sys} = 0.23), which shows the dynamic evolution of the boundary layer in the cycle. See Appendix A for further details.

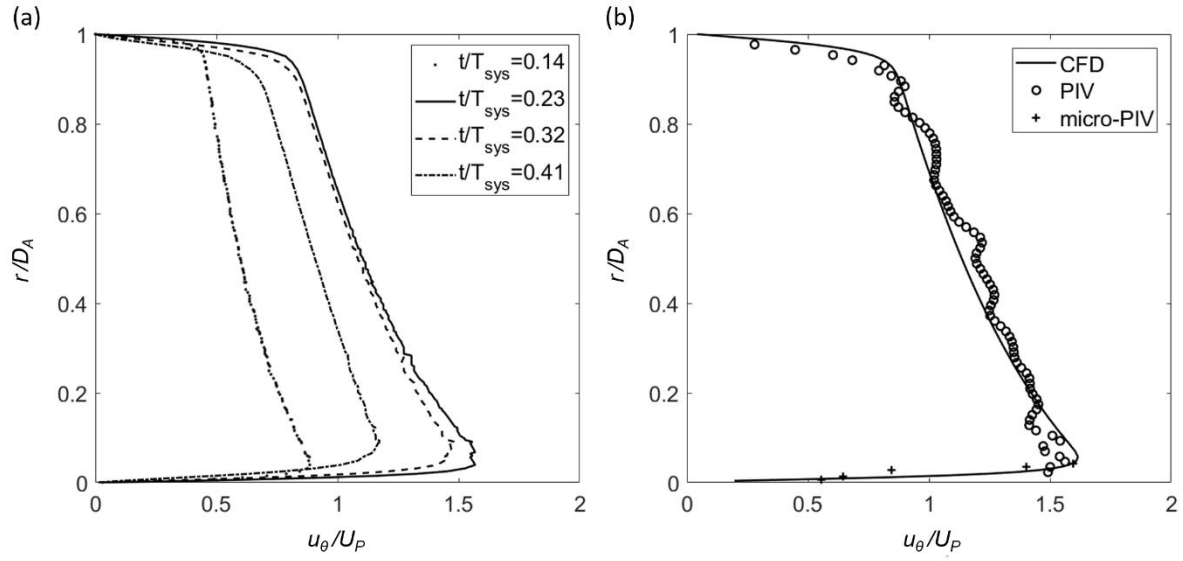

Figure 8. (a) Axial velocity profile evolution along the pulse, at the cross-section θ=21˚, on the centre plane AA', as predicted from CFD simulations. The vertical coordinate corresponds to the radial position along the cross-section of the aorta, measured from the inner wall towards the outer wall. (b) Comparison of experiment and CFD at one instant (t/T_{sys} = 0.23): Zoom-in PIV measurement of the core flow (open circular symbols), micro-PIV measurement at the near-wall region (plus-symbols).

The comparison of the instantaneous experimental data and the numerical velocity profiles presented in Figure 8b shows a good agreement in the core flow region. The experiments show some small-amplitude modulations, which are identified as peak-locking (Raffel et al., 2018a). Close to the walls, the results from the zoom-in PIV measurements show lack in spatial resolution, while the micro-PIV results are able to resolve the stronger gradients.

Figure 9 presents the evolution of the flow field in the ascending part of the aorta, as seen in the experiments and as predicted by the simulations. Experimental pathlines plotted as the trajectory of the tracer particles are compared with in-plane velocity and out-of-plane component of vorticity contours on the centre plane *AA'* of the CFD results. In the acceleration phase, the flow is homogeneous and remains fully attached to the walls of the ascending aorta. Later in the cycle, flow separation initiates on the inner wall at a location downstream of the apex (θ=90˚), which then develops and extends further while the separation point moves upstream. Still, the bulk of the flow remains laminar and attached to the outer wall until $0.63T_{sys}$, when a slender separation region can be observed near the entrance of the bend. Overall, for half of the systolic cycle until about $0.5T_{sys}$ the flow structure between experiment and CFD results show good agreement; it should be stressed that only the ramp-up part of the flow pulse ($0 < t < 0.2\ T_{sys}$) is relevant for the calibration. Therefore it should also not be surprising to notice differences to the experiments in the late phase of the flow pulse with separating shear layers, secondary vortices and stagnant zones, which is difficult to recapture with the laminar flow simulation.

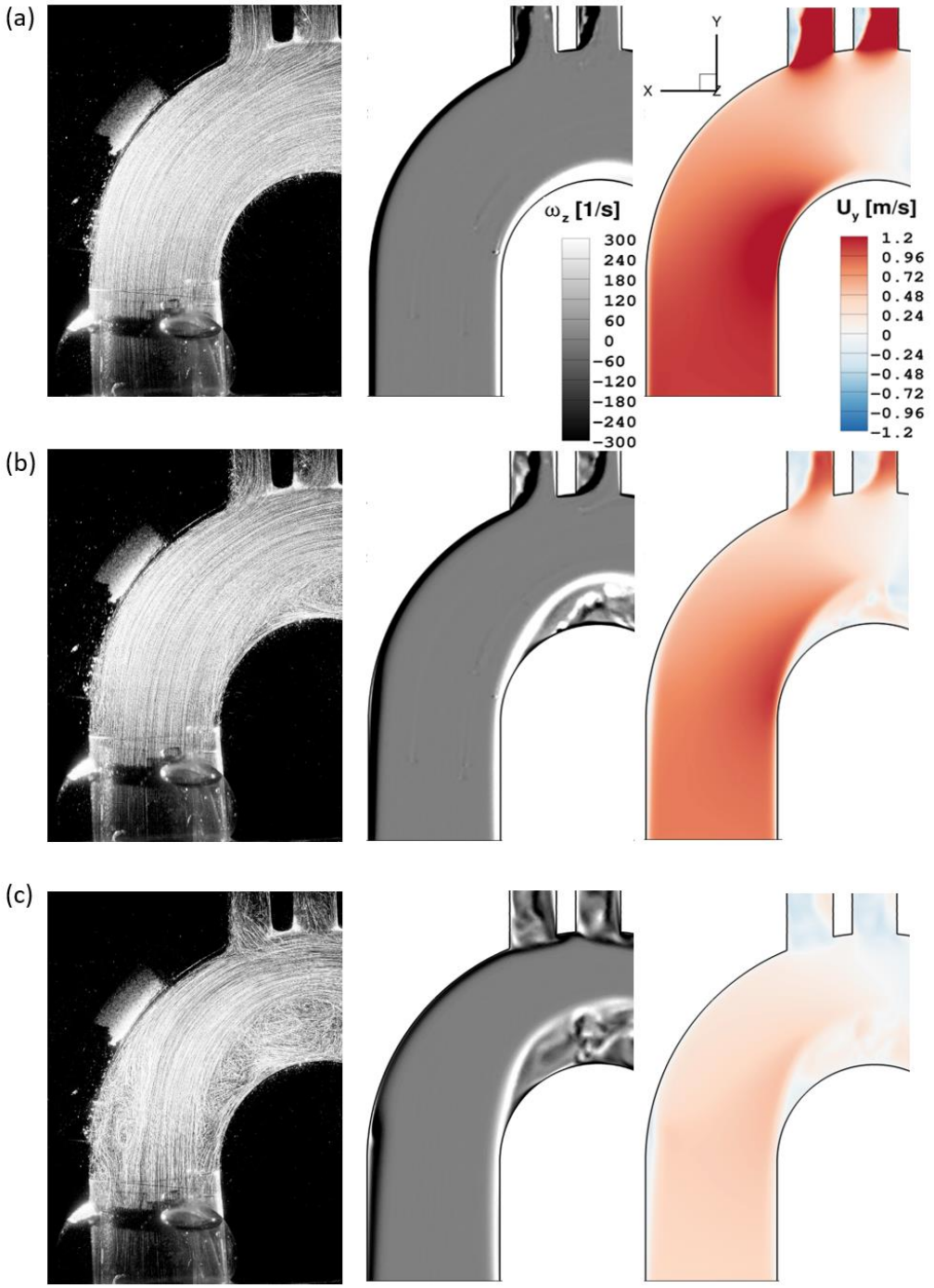

Figure 9. Flow pathlines (left column) extracted from the HS-PIV experiments, vorticity contours (middle column) and velocity contours (right column) along the centre plane AA', as derived from the CFD simulations, at (a) $0.23T_{sys}$, (b) $0.41T_{sys}$ and (c) $0.63T_{sys}$.

3.2 Parameter sensitivity analysis

To identify the parameters influencing the sensor sensitivity, we use the analytical methods described in section 2.1.3 in analogy to the derivations made for slender wind-hairs in the work from Dickinson (Dickinson, 2010). This is to understand the effect of velocity profile shape, boundary layer thickness and velocity magnitude on the sensitivity. The near-wall velocity profiles obtained from CFD are used as inputs into Eq. (5) and (6) for different times in the calibration pulse and the sensitivity S is calculated. The geometrical and material parameter are taken from the given sensor and the moment is calculated with the selected fluid parameter in the experiment. Iso-contours of the

sensitivity for the sensor at position θ=21˚ are given in Figure 10a as a function of the relative pillar length $l^* = L/\delta_2$ (ratio of pillar length to the boundary layer momentum thickness) and the characteristic free-stream velocity *U* (the velocity at the edge of the boundary layer). For relative low velocities in the early phase of the flow pulse, the dominant parameter for the sensitivity is the magnitude of the velocity itself (the sensitivity is low for the whole range of simulated pillar length). With increasing bulk flow velocity, the parameter of the boundary layer thickness gets of larger influence. The sensitivity is low when the relative pillar length is large (length l^*>15, i.e. the boundary layer thickness is thin with sharp velocity rise) or when it is very small (length l^*<2, i.e. the boundary layer thickness is very large with weak velocity rise). Thus the highest sensitivity appears in a certain range of the relative length values. For the flow condition investigated herein which is plotted in Figure 10a by the black line, we see that there is only slight change of the relative pillar length values from l^* =8 at the very beginning of the acceleration phase (~0.01T_{sys}) to l^* =4.3 at the peak systole (~0.23T_{sys}) for a large range of the characteristic velocity ($0< U < 1.5\ m/s$). Furthermore, the sensitivity reaches a plateau-like region when the characteristic velocity is above 1 m/s and for the full range of values of l^* covered herein. In this region the sensitivity remains within 90% of the maximum between the contours of the orange and red colored contour lines.

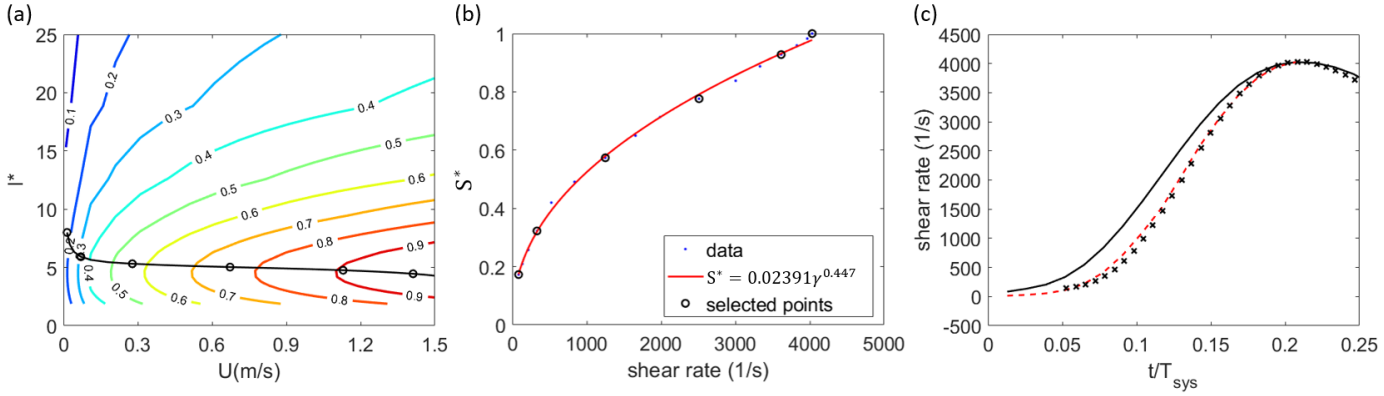

Figure 10. (a) Contours of the normalized sensitivity $S^* = S/S_{max}$ as a function of pillar length l^* and characteristic velocity *U* for the pillar sensor, overlaid with the plot of the evolution of l^* and U of the present pulsating flow condition obtained from CFD simulations at the acceleration phase and the peak systole, where S_{max} is the maximum value of the sensitivity which appears at the peak systole. (b) Plot of the normalized sensitivity relating to the shear rate fitted by Power Curve (R-square value of 0.9981). The black circle symbols denote the selected instantaneous values from 0.01T_{sys} to 0.21T_{sys} with a time increment of 0.04T_{sys}, which corresponds to the instantaneous data points (l^* ,*U*) shown as black circles in (a). (c) Temporal evolution of measured WS and CFD result in the calibration pulse (sensor position θ = 21° at the inner curvature of the arch). Symbols: experiment (only every fifth point); black solid line: CFD results; red dash line: CFD result with adapting the time-varying sensor sensitivity shown in (b).

Figure 10c displays exemplary the temporal WS signal for the sensor at the selected angle of θ= 21° in comparison to the CFD result at the acceleration phase and the peak systole, i.e. the laminar phase in the flow pulse. The temporal course of the sensor signal compared to the simulations illustrates an excellent overlap in the phase of peak systole, while the sensor is clearly underestimating the CFD data in the ramp-up phase. This is when strong acceleration of the bulk-flow near the entrance causes the boundary layer thickness to remain thin. By taking the sensitivity effect into account, i.e. correcting the shear rate values obtained from CFD by multiplying with the corresponding sensor sensitivity, we get an excellent overlap between the corrected CFD results with the values measured by the sensor. This gives us an indication on the measurement uncertainty in certain phases of the pulsating base flow.

3.3 Sensor response

The relationship of the sensitivity with the wall shear rate presented in Figure 10b is further used to illustrate the static response of the sensor. Figure 11 shows the measured tip deflection over the shear rate values from the CFD simulations, taken during the calibration pulse. It can be seen that the initial response at weak shear-rates is non-linear while for higher wall shear rate conditions the curve approaches a linear relationship, i.e. the range with approximately constant gain for flow condition with high shear rate values. This static response curve is later used to transfer the measured tip deflection to shear rate values.

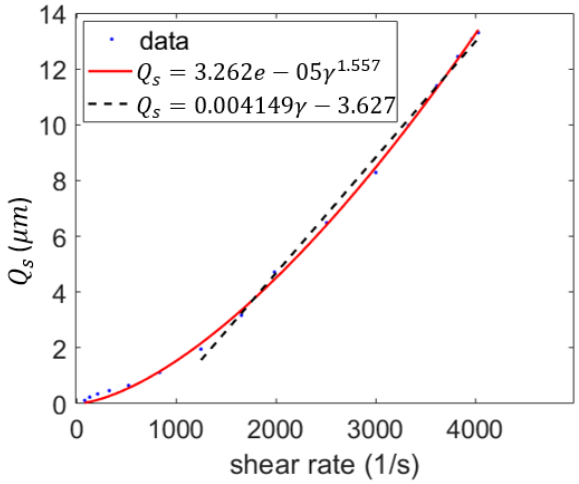

Figure 11. Static response of the micro-pillar sensor as pillar's tip displacement Q_s over the wall shear rate γ. The red line shows a Power Curve Fitting (R-square value of 0.9991), the black dash line shows a linear regression for the range $1250s^{-1} \leq \gamma \leq 4000s^{-1}$ (R-square value of 0.9953).

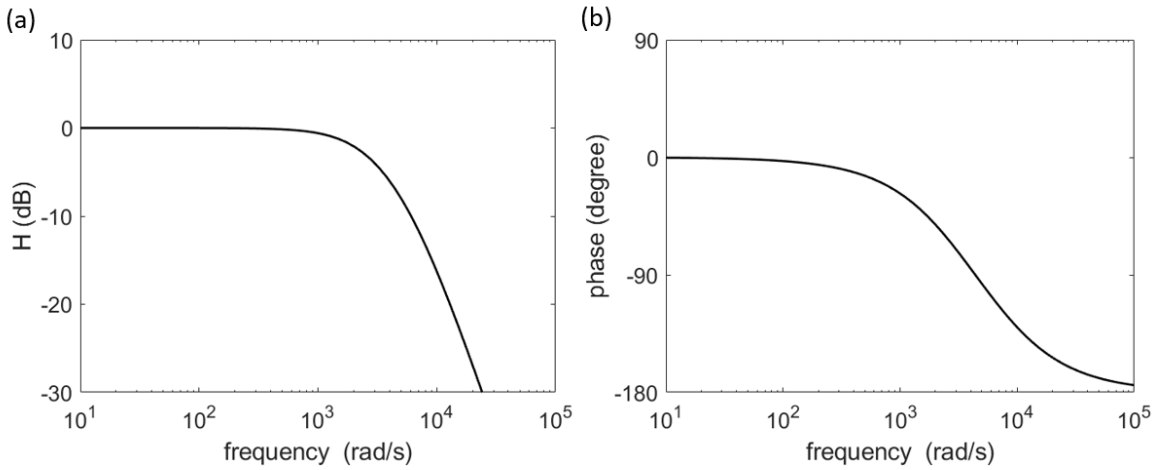

Figure 12. (a) and (b) gain and phase of the sensor response, obtained from the data of the acceleration phase in Figure 10c using an input-output response analysis.

Furthermore, the curves shown in Figure 10c are used to estimate the dynamic response of the sensors (see Figure 12) with the Matlab tool "procest" with 'P2' option (MATLAB® System Identification Toolbox™)(The MathWorks). This tool estimates the parameter for the 2nd order harmonic oscillator according to Eq. (1) in the time-domain from an input-output analysis (input: sensitivity-corrected CFD values, output: experimental values). The obtained transfer functions (gain and phase) are shown in Figure 12. The best fit with 93% prediction focus provides a natural frequency of ω_n =4386.6 rad/s and a Quality factor *Q*=0.459. First, the estimated natural frequency is in good agreement with the theoretical value given in section 2.1.3. Secondly, the quality factor clearly demonstrates the expected overdamped situation of the cantilever beam in the liquid environment. The response has a cut-off frequency f_C = 386 Hz when the gain is at 0.7071. At a frequency of 180 Hz, the gain is still 90% of its maximum with a phase lag of -30°. For frequencies below 120 Hz, the gain is better than 95% with a phase lag less than -20°. This is considered the measurement range of the sensor with near constant gain and a good representation of the dynamic change of the WS.

3.4 Case studies

The calibrated WS sensors are then used for mapping the spatio-temporal distribution of the WS at the inner curvature of the arch in the center plane. In the following, contours of constant streamwise WS are shown in plots with time as horizontal coordinate and the angular position displayed in the vertical coordinate.

3.4.1 Systolic flow with tubular insert

Figure 13 shows the spatio-temporal evolution of the WS distribution at the inner curvature of the arch for the complete systolic pulse. Because of the tubular insert (no valve), the flow is smooth and therefore also the distribution of the WS. It can be seen that the WS reaches the absolute peak value at the entrance to the arch (θ=17°) at the time of peak systole (0.25T_{sys}). However, the instant of peak WS is happening earlier in time the further we move up in the arch; this is seen by the peak location in the time axis moving further to the left. For example, at the largest angular position the peak occurs already at 0.2T_{sys}. The first indication of flow separation is seen at the apex of the aortic arch at 0.28-0.3T_{sys} by negative WS (blue color). The separation line between forward and retrograde flow (white color) further grows upstream over the deceleration phase along the curvature until it reaches the sinus region, which is consistent with the flow field shown in Figure 9. Later in the cycle at about 0.73T_{sys}, positive WS values re-appear in the separated region 56˚< θ<70˚ which indicates a local flow re-attachment. In the late phase > 0.9T_{sys} the flow along the inner curvature is retrograde all over the segment of the arch.

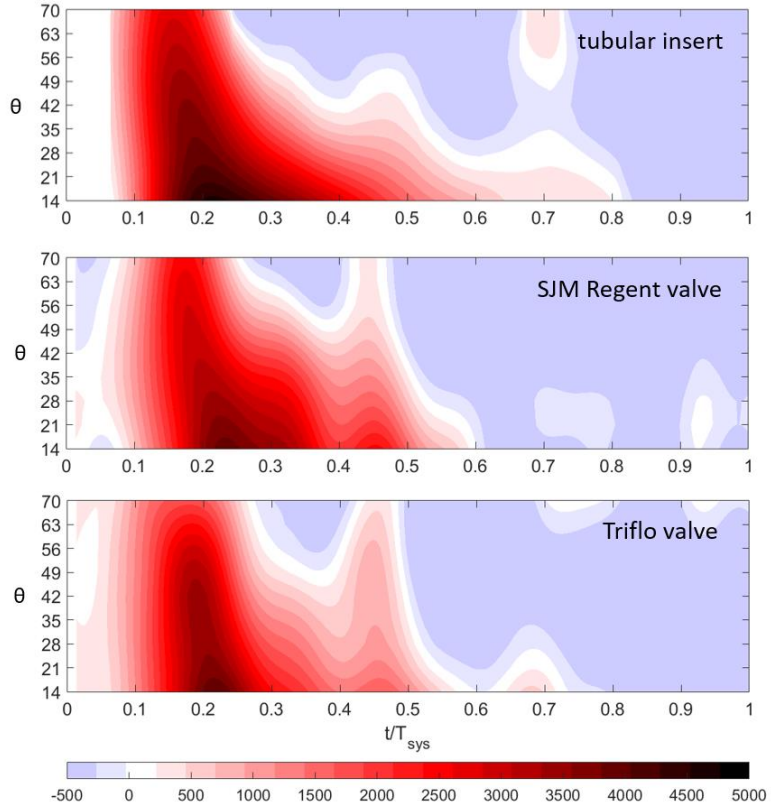

Figure 13. Spatio-temporal evolution of WS distribution along the inner curvature of the arch over the systolic flow pulse with tubular insert (sensor calibration configuration), shown by contours of constant WS (contours from blue: retrograde flow region with weak negative WS, to dark red: strong positive WS in streamwise direction).

3.4.2 Systolic flow with MHVs

The pillar sensors are applied to map the spatio-temporal evolution of streamwise WS along the inner curvature of the aortic arch induced by different MHVs. The flow field induced by both MHVs, i.e. SJM Regent valve and Triflo valve, has been detailed in our previous study (Li et al., 2020). The spatio-temporal evolution of the WS distribution at the inner curvature of the arch is shown in Figure 13. Slightly negative wall shear rate values are seen at the beginning of the systolic cycle for SJM Regent valve. This indicates that there is a backward flow along the inner curvature wall, which may link to the opening of the SJM Regent valve when the leaflet facing the inner curvature rotates from the valve housing to center along the hinge. This is not shown for Triflo valve because the opening of its leaflet is from center to outside. Thereafter, a first significant peak occurs for both valves at 0.2T_{sys}, the value of which is comparable to the WS peak value generated in the calibration pulse. It indicates that this peak is induced by the wash-out flow at the beginning of the systolic cycle. As seen from the spatio-temporal plot, the impact is rather a short-lived event as the duration is about 0.05T_{sys}. Later, a higher peak occurs for both valves at the entrance to the arch at about peak

555 systole. This is generated by the side orifice jets of the MHVs when they impact with the wall. From then on, the Triflo
556 valve generates no further significant WS peaks, while the SJM Regent valve keeps high WS values until $0.35T_{sys}$. These
557 results hint on a lower impact of the Triflo valve regarding the generation of excessive fluctuating WS stresses on the
558 aortic wall related to the valve design. In addition, it is seen that the SJM Regent valve generates overall elevated levels
559 of WS in the deceleration phase along the inner curvature. Clear indications of retrograde flow are found starting at
560 the most downstream location at about $0.5T_{sys}$. The backflow regions with negative streamwise WS are larger extended
561 for the SJM Regent valve compared to the Triflo valve.
562
563 **4. Discussion**

564 Micro-pillar WSS sensors have a certain measuring range and accuracy depending on their size and flexural
565 stiffness, besides other factors such as their sensitivity. In addition, their length relative to the thickness of the
566 boundary layer is an important aspect affecting the measurement. As they belong to the class of indirect sensors, they
567 need an accurate calibration under representative and repeatable flow conditions (Bruecker et al., 2007). This task
568 may be difficult if the sensors are applied in complex geometries and/or in complex flows with oscillating boundary
569 layers, separating flows and strongly curved streamlines. Such a situation is the pulsating flow in the aortic arch where
570 in-vitro measurements of the WS are highly welcome to investigate the potential damage of valve-induced jets
571 impacting with the aortic walls. An ex-situ calibration with the sensors outside the model might be not reliable for the
572 following reasons: a) the clamping conditions of the micro-pillar at the wall can be different ex-situ and in-situ; b) the
573 foot could be not flush with the wall, due to inaccurate assembling; c) the micro-pillar may not be perpendicular to
574 the wall, e.g. already bent to one side; d) the shape and mechanical properties of the micro-pillar may have changed
575 over time. All the factors mentioned above could influence the accuracy of the measuring system. Therefore, the best
576 practice is to do the calibration in-situ in the same environment. However, even then the reference data necessary to
577 determine the flow field around the pillars may not be easy to obtain, either from flow field measurements or from
578 alternative measurement methods. Herein, CFD simulations are used to provide the required reference data for the
579 calibration of the experiment in a special configuration: the aortic valve in the phantom is replaced with a tubular
580 insert (smooth bend) and a single flow pulse is imposed, the same simulated with CFD at identical boundary conditions.
581 An important aspect of the employed simulations is the automatic grid generation and the cost-effective laminar
582 calculations for the acceleration part of the pulse, which make them practical for the calibration of the measurement
583 apparatus.

584 For the calibration, the results show that the length of the sensor and the bulk flow velocity magnitude lead to a
585 time-varying sensitivity in the situation of strong variation of mean flow with oscillating boundary layers such as in the
586 herein studied pulsating flow. The sensitivity of the applied sensors is low in regions of thin boundary layers or to times
587 of low velocity magnitude, whereas it increases towards a rather constant plateau for higher velocities in the range of
588 peak systole (flow velocities 1-1.5m/s) for all relative pillar length in the span of 2-7. Excellent agreement to the
589 measured data is found in the pulse-type calibration flow for all instants when the effect of the varying sensitivity is
590 taken into account in the simulated data. This allowed us to determine the static and dynamic response of the sensors.
591 With that, we can estimate the uncertainty of different length of sensors and develop design rules for best practice in
592 using such sensors for future measurements. As a direct result of this study, we can understand why our previous
593 measurements with 1 mm length micro-pillar sensors in the silicone model reported in (Li et al., 2020) might have
594 resulted in overall lower WS values with potential underestimation of peak WS values of more than 50%. In addition,
595 it cannot be excluded that the previously used silicone model had somewhat softer clamping conditions at the root of
596 the sensors as for the Perspex model used herein. Finally, it became obvious that the material properties of the original
597 sensors degraded over time, which requires to update the calibration data from measurements to measurement. With
598 the methodology proposed herein, there is no need to update the reference data as the simulation conditions have
599 not changed.

600 For the investigated heart valves the results hint on a lower impact of the Triflo valve compared to the SJM Regent
601 regarding the generation of excessive fluctuating WS stresses on the aortic wall. In addition, it is seen that the SJM
602 Regent valve generates overall elevated levels of WS in the deceleration phase along the inner curvature. Clear
603 indications of retrograde flow are found starting at the most downstream location at about $0.5T_{sys}$. The backflow
604 regions with negative streamwise WS are larger extended for the SJM Regent valve compared to the Triflo valve.
605
606

5. Conclusions

A method is presented for CFD-assisted in-situ calibration of micro-pillar WSS sensors when used for in-vitro studies of pulsating flow in the complex geometry of the aortic arch. Experimental measurements of spatio-temporal WSS maps are reported in a model of the human aorta with arrays of micro-pillar WSS sensors along the symmetry plane of the bend. The results allow quantification of the impact of heart-valve prostheses on the flow-imposed stresses along the aortic wall. A laminar flow pulse is used to calibrate the sensors in-situ with reference data from CFD simulations under equivalent boundary conditions. This method overcomes the problem of limited accuracy when the sensors are calibrated ex-situ, in other flow conditions not relevant for the current flow situation or when errors are introduced by inaccurate positioning or clamping conditions. The results show the importance of the integration effect of the length of the micro-pillar sensors, which induces uncertainties in thin boundary layers, which can be quantified now. Furthermore, the reconstructed static response allows to correct for weak sensitivities in phases of weak mean flow. Calibrated micro-pillar sensors of 500 µm length are then employed to map the spatio-temporal evolution of WS along the inner curvature of the aorta induced by two different MHVs. It has been found that the SJM Regent valve generates higher fluctuation amplitudes of the WS for a longer duration during the systolic phase than the Triflo valve. In addition, stronger retrograde flow is generated. The results help to qualify the selection of different designs also with regards to the impact those valves have on the stresses along the aortic wall. Future measurements with the same pulse-duplicator and measurement technique allow also to address bioprostheses or transcatheter aortic valve implantation (TAVI). Furthermore, the image processing step can be converted online by using modern FPGA-based digital cameras with on-board tracking features. This would allow to track the spots of the sensor tips simultaneously and streaming the data online, while the further signal processing can be done on the fly using standard subtracting and filtering methods. With this further enhancement, the valve tester can directly visualize the impact of the heart valve on the distal walls on a display overlaid with the contours and the WS information. This represents a further step towards a more sophisticated quality control of valve design and implantation techniques using such a valve tester.

CRediT authorship contribution statement

Qianhui Li: Methodology, Software, Validation, Formal Analysis, Investigation, Resources, Visualization, Data Curation, Writing – Original Draft; Writing – Review & Editing. **Evangelos Stavropoulos-Vasilakis:** Methodology, Software, Validation, Visualization, Data Curation, Writing – Original Draft. **Phoevos Koukouvinis:** Supervision, Software, Writing – Review & Editing. **Manolis Gavaises:** Stewardship, Funding acquisition, Resources, Supervision, Writing – Review & Editing. **Christoph H. Bruecker:** Stewardship, Project Administration, Funding acquisition, Resources, Conceptualization, Methodology, Software, Writing – Original Draft; Writing – Review & Editing

Acknowledgements

Prof. Bruecker holds the BAE SYSTEMS Sir Richard Olver Chair in Aeronautical Engineering and the Royal Academy of Engineering Research Chair in Nature-inspired flow sensing and manipulation. The position is co-sponsored by BAE SYSTEMS and the Royal Academy of Engineering [Grant number RCSRF1617\4\11], which is gratefully acknowledged herein. The position of Dr Qianhui Li is funded by The Engineering and Physical Sciences Research Council (EPSRC) project [EP/T006315/1], which is also gratefully acknowledged herein. Dr. E. Stavropoulos-Vasilakis worked within the framework of CaFE project, which received funding from the European Union Horizon 2020 Research and Innovation programme [Grant number 642536]. The authors would like to thank Dr Andreas Papoutsakis for the thorough scientific discussion on CFD during this study, Dr Homa Naseri for the help regarding meshing strategy. The authors would also like to express our thanks to the Helmholtz Institute of RWTH Aachen University, Germany, for providing the SJM Regent valve and Novostia SA, Neuchâtel, Switzerland for the Triflo valve used in this project.

Funding

This work was supported by BAE SYSTEMS and the Royal Academy of Engineering [Grant number RCSRF1617\4\11], both jointly funding the position of Professor Christoph Bruecker; The position of Dr Qianhui Li is funded by The Engineering and Physical Sciences Research Council (EPSRC) project [EP/T006315/1]; Dr. E. Stavropoulos-Vasilakis worked within the framework of CaFE project, which received funding from the European Union Horizon 2020 Research and Innovation programme [Grant number 642536].

References

Andriotis, A., Zifan, A., Gavaises, M., Liatsis, P., Pantos, I., Theodorakakos, A., Efstathopoulos, E.P., Katritsis, D., 2008. A new method of three‐dimensional coronary artery reconstruction from X‐ray angiography: Validation against a virtual phantom and multislice computed tomography. Catheterization and cardiovascular interventions 71, 28-43.

Bodnár, T., Sequeira, A., Prosi, M., 2011. On the shear-thinning and viscoelastic effects of blood flow under various flow rates. Applied Mathematics and Computation 217, 5055-5067.

Borazjani, I., Ge, L., Sotiropoulos, F., 2008. Curvilinear immersed boundary method for simulating fluid structure interaction with complex 3D rigid bodies. Journal of Computational physics 227, 7587-7620.

Bruecker, C., Bauer, D., Chaves, H., 2007. Dynamic response of micro-pillar sensors measuring fluctuating wall-shear-stress. Experiments in fluids 42, 737-749.

Bruecker, C., Spatz, J., Schröder, W., 2005. Feasability study of wall shear stress imaging using microstructured surfaces with flexible micropillars. Experiments in fluids 39, 464-474.

Chien, S., Li, S., Shyy, J.Y., 1998. Effects of mechanical forces on signal transduction and gene expression in endothelial cells. Hypertension 31, 162-169.

Corso, P., Walheim, J., Dillinger, H., Giannakopoulos, G., Gülan, U., Frouzakis, C.E., Kozerke, S., Holzner, M., 2021. Toward an accurate estimation of wall shear stress from 4D flow magnetic resonance downstream of a severe stenosis. Magnetic Resonance in Medicine.

Dasi, L., Ge, L., Simon, H., Sotiropoulos, F., Yoganathan, A., 2007. Vorticity dynamics of a bileaflet mechanical heart valve in an axisymmetric aorta. Physics of Fluids 19, 067105.

De Tullio, M., Cristallo, A., Balaras, E., Verzicco, R., 2009. Direct numerical simulation of the pulsatile flow through an aortic bileaflet mechanical heart valve. Journal of Fluid Mechanics 622, 259-290.

Dickinson, B., Singler, J., Batten, B., 2012. Mathematical modeling and simulation of biologically inspired hair receptor arrays in laminar unsteady flow separation. Journal of Fluids and Structures 29, 1-17.

Dickinson, B.T., 2010. Hair receptor sensitivity to changes in laminar boundary layer shape. Bioinspiration & biomimetics 5, 016002.

Fung, Y.-c., 2013. Biomechanics: mechanical properties of living tissues. Springer Science & Business Media.

Gülan, U., Holzner, M., 2018. The influence of bileaflet prosthetic aortic valve orientation on the blood flow patterns in the ascending aorta. Medical engineering & physics 60, 61-69.

Ge, L., Dasi, L.P., Sotiropoulos, F., Yoganathan, A.P., 2008. Characterization of hemodynamic forces induced by mechanical heart valves: Reynolds vs. viscous stresses. Annals of Biomedical Engineering 36, 276-297.

Gross-Hardt, S., Boehning, F., Steinseifer, U., Schmitz-Rode, T., Kaufmann, T., 2018. Mesh sensitivity analysis for quantitative shear stress assessment in blood pumps using computational fluid dynamics. Journal of biomechanical engineering.

Haruguchi, H., Teraoka, S., 2003. Intimal hyperplasia and hemodynamic factors in arterial bypass and arteriovenous grafts: a review. Journal of Artificial Organs 6, 227-235.

Howarth, L., 1938. On the solution of the laminar boundary layer equations. Proceedings of the Royal Society of London. Series A-Mathematical and Physical Sciences 164, 547-579.

Iasiello, M., Vafai, K., Andreozzi, A., Bianco, N., 2016. Analysis of non-Newtonian effects on low-density lipoprotein accumulation in an artery. Journal of biomechanics 49, 1437-1446.

Iasiello, M., Vafai, K., Andreozzi, A., Bianco, N., 2017. Analysis of non-Newtonian effects within an aorta-iliac bifurcation region. Journal of biomechanics 64, 153-163.

Jana, A., Raman, A., Dhayal, B., Tripp, S.L., Reifenberger, R.G., 2007. Microcantilever mechanics in flowing viscous fluids. Applied Physics Letters 90, 114110.

Katritsis, D., Kaiktsis, L., Chaniotis, A., Pantos, J., Efstathopoulos, E.P., Marmarelis, V., 2007. Wall shear stress: theoretical considerations and methods of measurement. Progress in cardiovascular diseases 49, 307-329.

Katritsis, D., Theodorakakos, A., Pantos, I., Andriotis, A., Efstathopoulos, E., Siontis, G., Karcanias, N., Redwood, S., Gavaises, M., 2010. Vortex formation and recirculation zones in left anterior descending artery stenoses: computational fluid dynamics analysis. Physics in Medicine & Biology 55, 1395.

Katritsis, D.G., Theodorakakos, A., Pantos, I., Gavaises, M., Karcanias, N., Efstathopoulos, E.P., 2012. Flow patterns at stented coronary bifurcations: computational fluid dynamics analysis. Circulation: Cardiovascular Interventions 5, 530-539.

Kim, T., Cheer, A., Dwyer, H., 2004. A simulated dye method for flow visualization with a computational model for blood flow. Journal of biomechanics 37, 1125-1136.
Kunze, S., Chaves, H., Brücker, C., 2008. Mirror particle-tracking-velocimetry in a strip-coded light-sheet: a new method to determine the wall-shear-stress field. Experiments in fluids 45, 573-581.
Lantz, J., Renner, J., Karlsson, M., 2011. Wall shear stress in a subject specific human aorta—influence of fluid-structure interaction. International Journal of Applied Mechanics 3, 759-778.
Li, Q., Bruecker, C.H., 2018. Vortex interaction with a rough wall formed by a hexagonal lattice of posts. Physics of Fluids 30, 054107.
Li, Q., Hegner, F., Bruecker, C.H., 2020. Comparative study of wall-shear stress at the ascending aorta for different mechanical heart valve prostheses. Journal of biomechanical engineering 142.
Markl, M., Wallis, W., Harloff, A., 2011. Reproducibility of flow and wall shear stress analysis using flow‐sensitive four‐dimensional MRI. Journal of Magnetic Resonance Imaging 33, 988-994.
Marrero, V.L., Tichy, J.A., Sahni, O., Jansen, K.E., 2014. Numerical study of purely viscous non-Newtonian flow in an abdominal aortic aneurysm. Journal of biomechanical engineering 136.
Mittal, R., Simmons, S., Najjar, F., 2003. Numerical study of pulsatile flow in a constricted channel. Journal of Fluid Mechanics 485, 337-378.
Moukalled, F., Mangani, L., Darwish, M., 2016. The finite volume method in computational fluid dynamics. An Advanced Introduction with OpenFOAM and Matlab, 3-8.
Orlü, R., Vinuesa, R., 2020. Instantaneous wall-shear-stress measurements: advances and application to near-wall extreme events. Measurement Science and Technology.
Papathanasopoulou, P., Zhao, S., Köhler, U., Robertson, M.B., Long, Q., Hoskins, P., Yun Xu, X., Marshall, I., 2003. MRI measurement of time‐resolved wall shear stress vectors in a carotid bifurcation model, and comparison with CFD predictions. Journal of Magnetic Resonance Imaging 17, 153-162.
Pinto, S., Romano, E., António, C., Sousa, L., Castro, C., 2020. The impact of non-linear viscoelastic property of blood in right coronary arteries hemodynamics—a numerical implementation. International Journal of Non-Linear Mechanics 123, 103477.
Politi, M.T., Ghigo, A., Fernández, J.M., Khelifa, I., Gaudric, J., Fullana, J.M., Lagrée, P.-Y., 2016. The dicrotic notch analyzed by a numerical model. Computers in biology and medicine 72, 54-64.
Potters, W.V., Marquering, H.A., VanBavel, E., Nederveen, A.J., 2014. Measuring wall shear stress using velocity-encoded MRI. Current Cardiovascular Imaging Reports 7, 9257.
Prandtl, L., 1952. Essentials of Fluid Dynamics, Hafner Publ. Co., New York, 117.
Raffel, M., Willert, C.E., Scarano, F., Kähler, C.J., Wereley, S.T., Kompenhans, J., 2018a. Particle image velocimetry: a practical guide. Springer.
Raffel, M., Willert, C.E., Scarano, F., Kähler, C.J., Wereley, S.T., Kompenhans, J., 2018b. Techniques for 3D-PIV, Particle Image Velocimetry: A Practical Guide. Springer International Publishing, Cham, pp. 309-365.
Raghav, V., Sastry, S., Saikrishnan, N., 2018. Experimental Assessment of Flow Fields Associated with Heart Valve Prostheses Using Particle Image Velocimetry (PIV): Recommendations for Best Practices. Cardiovascular engineering and technology, 1-15.
Shaaban, A.M., Duerinckx, A.J., 2000. Wall shear stress and early atherosclerosis: a review. American Journal of Roentgenology 174, 1657-1665.
Stankovic, Z., Allen, B.D., Garcia, J., Jarvis, K.B., Markl, M., 2014. 4D flow imaging with MRI. Cardiovascular diagnosis and therapy 4, 173.
Stettler, J., Hussain, A.F., 1986. On transition of the pulsatile pipe flow. journal of fluid mechanics 170, 169-197.
The MathWorks, I., Fourier Series, Natick, Massachusetts, United State.
The MathWorks, I., System Identification Toolbox, Natick, Massachusetts, United State.
Trip, R., Kuik, D., Westerweel, J., Poelma, C., 2012. An experimental study of transitional pulsatile pipe flow. Physics of fluids 24, 014103.
Tu, J., Inthavong, K., Wong, K.K.L., 2015. Computational Hemodynamics–Theory, Modelling and Applications. Springer.
Van Eysden, C.A., Sader, J.E., 2006. Resonant frequencies of a rectangular cantilever beam immersed in a fluid. Journal of applied physics 100, 114916.
Weller, H.G., Tabor, G., Jasak, H., Fureby, C., 1998. A tensorial approach to computational continuum mechanics using object-oriented techniques. Computers in physics 12, 620-631.

768 Xu, D., Warnecke, S., Song, B., Ma, X., Hof, B., 2017. Transition to turbulence in pulsating pipe flow. Journal of Fluid
769 Mechanics 831, 418-432.
770 Yuce, M.I., Kareem, D.A., 2016. A numerical analysis of fluid flow around circular and square cylinders. Journal -
771 American Water Works Association 108, E546-E554.
772 Zimmermann, J., Demedts, D., Mirzaee, H., Ewert, P., Stern, H., Meierhofer, C., Menze, B., Hennemuth, A., 2018. Wall
773 shear stress estimation in the aorta: Impact of wall motion, spatiotemporal resolution, and phase noise. Journal of
774 Magnetic Resonance Imaging.

775

776

Appendices

Appendix A

Description of flow

As shown in Figure 8a, at location θ = 21°, the boundary thickness grows from near zero to about 0.5 mm at the very beginning of the ramp (t/T_{sys}=0.07), about 1 mm at t/T_{sys} = 0.14 and reaches a thickness of about 1.5 mm at the peak systole; Eventually, it is growing then further due to the adverse pressure gradient in the deceleration phase. The evolution of the boundary layer displacement thickness $\delta_1 = \int_0^{\delta_{max}} (1 - u/U)\, dr$ and momentum thickness $\delta_2 = \int_0^{\delta_{max}} u/U\,(1 - u/U)\, dr$ at the acceleration phase is shown in Figure A.1a and Figure A.1b respectively, where upper integral limit δ_{max} is the location of the velocity peak of the instant velocity profile U. The boundary layer shape is further quantified with the Hartree shape factor, $H = \delta_1/\delta_2$, of which the evolution is shown in Figure A.1c. It can be seen that the values of the Hartree shape factor remains similar magnitude over the time with an average value of H =2.5. According to (Dickinson, 2010), *H* = 4.029 represents laminar separation, H=2.591 corresponds to Blasius flow (flow over a flat plate) and *H* =2.216 indicates flow to a plane stagnation point (Hiemenz flow). It indicates that the flow condition of the present study at the acceleration phase and the peak systole resembles the Blasius flow and could be theoretically analyzed using Blasius solution.

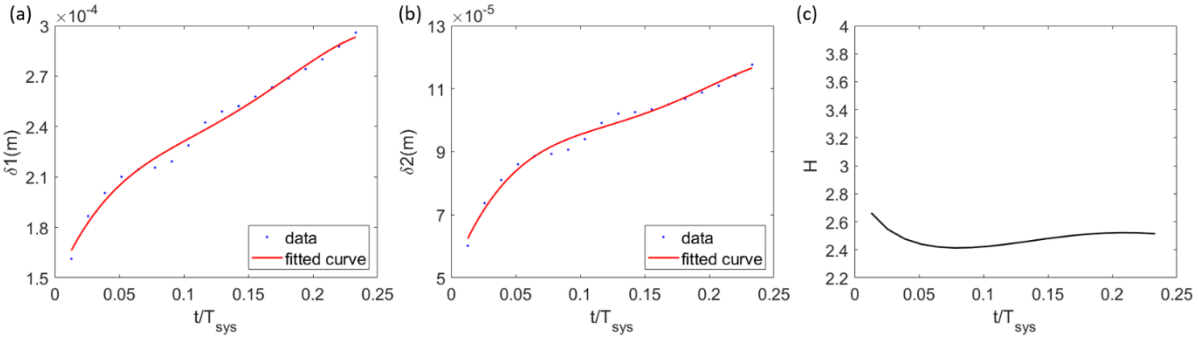

Figure A.1. Plots of the evolution of a) the displacement boundary layer thickness δ_1, b) the momentum boundary layer thickness δ_2, and c) the Hartree shape factor $H = \delta_1/\delta_2$ over the acceleration phase obtained from CFD simulations.

To analyze the sensitivity of the sensor in near wall flow with developing boundary layer, we simulate the flow condition described by Blasius flow along a flat plate at zero incidence (Howarth, 1938) which is governed by the Blasius equation $ff''+2f''' = 0$ with the boundary conditions $f(0) = f'(0) = 0$, $f'(\infty) = 1$.

The wall shear rate of Blasius flow is calculated as (Howarth, 1938)

$$\gamma = (\frac{\partial u}{\partial y})_{y=0} = 0.332U\sqrt{\frac{U}{\nu x}}, \tag{A.1}$$

where *x* is the position from the leading edge which calculated from the Blasius solution table, using the dimensionless coordinate $\eta = y\sqrt{\frac{U}{\nu x}} = 5$ at u/U=0.99155.

We investigate on a range of values of the free stream velocity U varying from $0.01\ m/s$ to $1.5\ m/s$ with a step of 0.01 m/s ; For each U, by varying the position from the leading edge, we obtained the corresponding flow profile with a series of boundary layer thickness δ_{99} $(0.02\ mm \le \delta_{99} \le 2\ mm, i.e.\ 0.25 \le l^* \le 25)$. Thus we obtained a series of self-similar flow profiles, which is applied to investigate on the sensitivity of the sensor, assuming that the presence of the pillar has little effect on the surrounding upstream flow.

Appendix B

Rheology of Blood

In the simulations the working fluid is considered Newtonian. On the one hand, this modelling strategy is followed in order to replicate the conditions of the experiment, which is intended to provide a new kind of heart valve tester with potential use for FDA regulation with regards to critical WSS distal of MHV. Non-Newtonian fluid effects are expected to play a minor role for the specific problem of larger vessel studies such as the pulsatile flow through the aorta. Numerous studies have examined the flow distribution in arteries and arterial trees, considering realistic

geometries derived from X-ray angiograms as well as in the carotid artery; indicative early work from the research groups (Andriotis et al., 2008; Katritsis et al., 2010; Katritsis et al., 2012) as well as more recent from Iasiello et al. (Iasiello et al., 2016, 2017) suggest that for large blood vessel dimensions such as the aorta, non-Newtonian effects play minor role to the overall flow distribution; they become more important for smaller or stenosed vessels (Bodnár et al., 2011; Iasiello et al., 2016; Marrero et al., 2014; Pinto et al., 2020) and at time instances where recirculation zones are formed (Iasiello et al., 2016; Marrero et al., 2014) or at regions where high-velocity gradients are encountered (Pinto et al., 2020). The use of the water-glycerine mixture in the experiment and its comparison to the rheology of blood has been also discussed in our previous work (Li et al., 2020).

Grid Independence

An automatic unstructured tetrahedral grid generation process is chosen for the discretization of the computational domain. The inputs are limited to the CAD geometry of the aorta model and the desired cell size. Initially, the surface representing the aorta walls is triangulated; then the structured layers are created, which have a triangular base on the wall and thus, a prismatic shape; finally the volume is filled with unstructured tetrahedra.

In order to assess the influence of spatial resolution on the numerical calculations of the pulsatile flow under consideration and on the estimation of the WS, a grid independence study has been performed. Three different unstructured tetrahedral meshes, shown in Figure B.1, have been used with a total cell count of 2, 9 and 11 million cells, refereed as coarse, middle and fine meshes, respectively. The spatial resolution of the three meshes is listed in Table B.1. All feature additional prism layers near the wall covering the pillars, which controls better the cell height growth away from the wall and assists in better capturing the boundary layer. There are 10 layers for the coarse and medium meshes and 15 layers for the fine mesh, with a growth factor of 1.2 and a first cell height obeying the condition $y_+ \leq 1$.

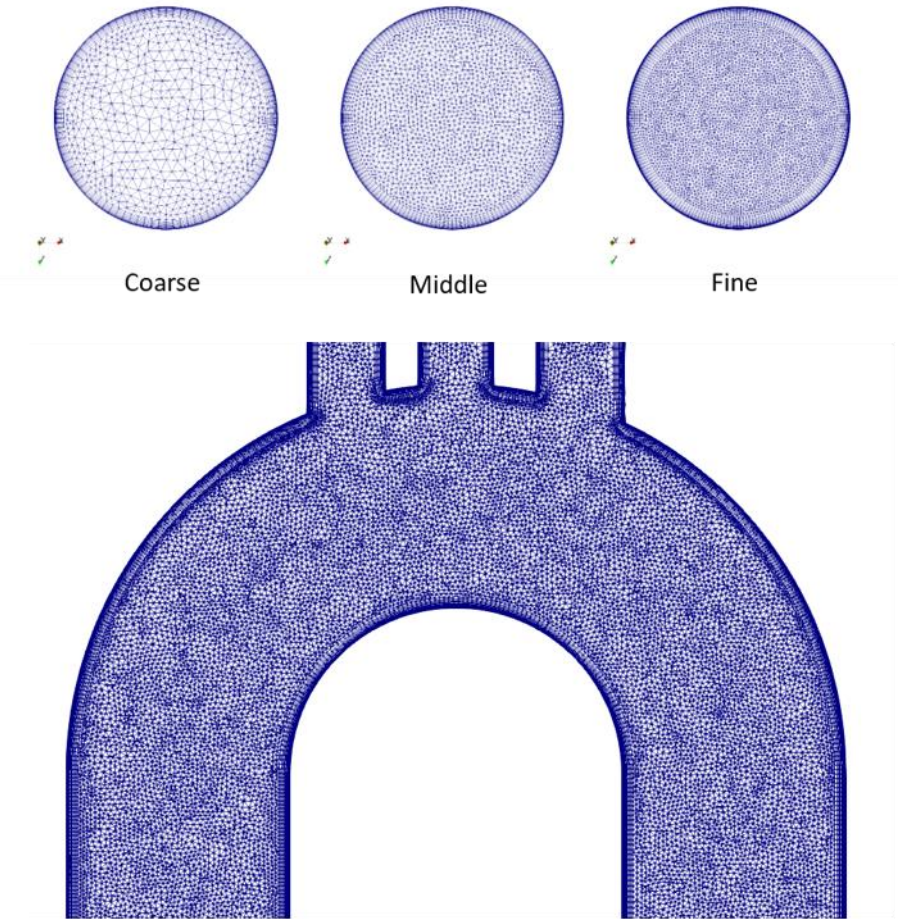

Middle – AA' plane

Figure B.1. Top: Cross-section slice of the mesh, on the beginning of the aorta bend (θ=0˚). Bottom: Slice on the central plane AA' of the middle mesh, focused on the aortic arc and the roots of the arterial bifurcations. All three grids are unstructured tetrahedral grids, with additional layers of prism cells in the near-wall region to better resolve the boundary layer of the flow. The coarse grid is composed by 2 million cells, the medium by 9 million cells and the fine by 11 million cells.

Table B.1. Resolution and computational cost of the three meshes used for the grid independence study. Along with the total number of cells, the table shows the cell characteristic length along the aortic arc (dl_{arc}), on the circumference of the aorta (dl_{circ}), in the core volume over the layers (h_{core}) and the first cell height on the wall, with respect to the y_+ rule (y_1/y_1^*), as well as the number of nodes on the circumference of the aorta (N_{circ}). Herein $y_1^* = 59.4\mu m$, for *Re*=5415, corresponding to the peak velocity.

Mesh Name	Cell Number	dl_{arc}	dl_{circ}	h_{core}	y_1/y_1^*	N_{circ}	CPUh
Coarse	2M	$D_A/42$	$D_A/21$	$D_A/63$	0.66	180	3531
Medium	9M	$D_A/57$	$D_A/44$	$D_A/97$	0.66	248	41493
Fine	11M	$D_A/77$	$D_A/63$	$D_A/120$	0.33	324	55509

Figure B.2 compares CFD results obtained for the three different grids. The velocity profiles along the diameter of the aorta demonstrate convergence of the numerical predictions. Although the velocity of the bulk flow is slightly distorted for the coarse mesh, it follows closely the results of the other grids. In conclusion, it can be argued that the medium mesh (9 million cells) gives grid independent results for the near-wall velocity gradients along the aortic wall.

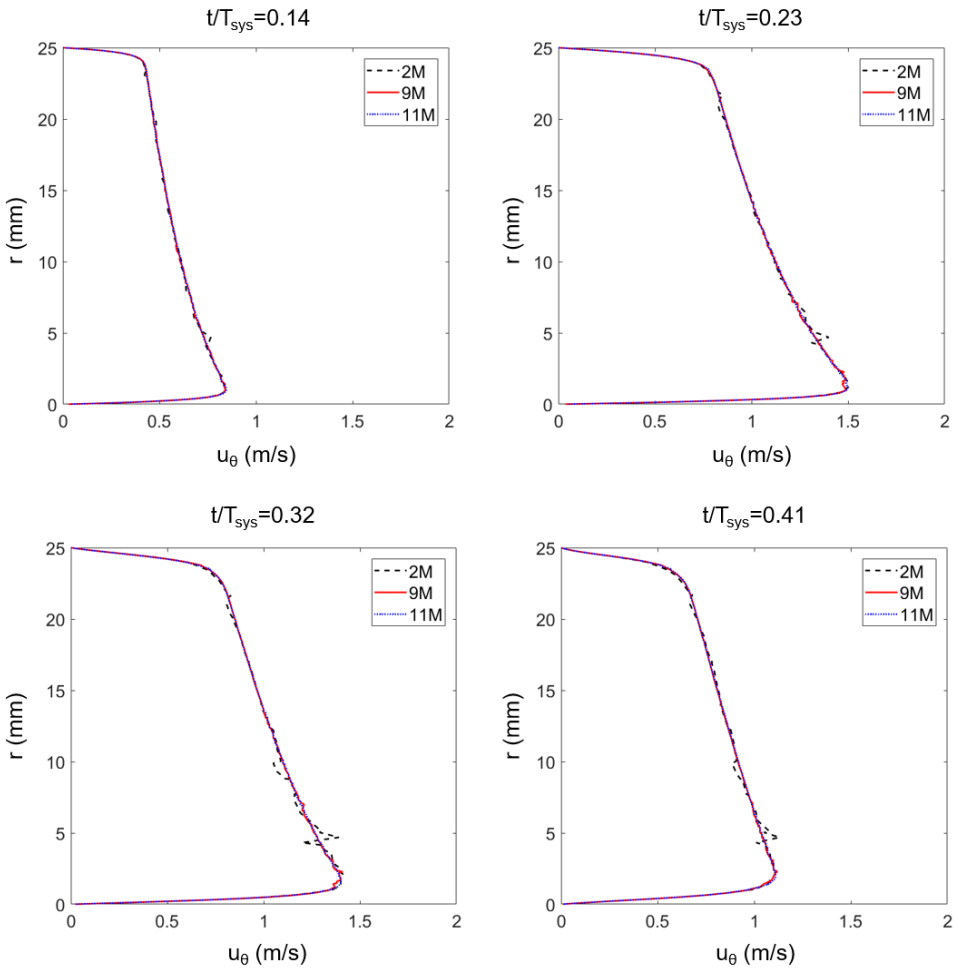

Figure B.2. Profiles of the tangential velocity $u_\theta(r)$ in the bend corresponding to cross-section $\theta=21^\circ$ at the centre plane. Results for the three different grids are shown, where T_{sys} is the period of the systolic cycle.

Grid generation

The generation of this type of grids is fast, simple and straightforward and requires little involvement of the user. An alternative would be to use a structured hexahedral mesh, which would especially lead to a lower number of cells. However the creation of such grids, in a non-automated "blocked mesh" approach, would be challenging and importantly more time consuming. The arterial branches on top of the apex of the aorta pose a complex topological constraint to the structured hexahedral grids. Moreover, the automatic generation of a hexahedral-dominant grid may seem a promising option, however the resulting mesh may not be of great quality, especially when layering is used for the boundary layer region. The tetrahedral grid generation process employed ensures smooth transition from the structured layers to the unstructured core of the mesh. Finally, automatic hexahedral mesh generation remains a numerical challenge.

Spatial resolution

For pulsatile aortic flows, which usually reach a peak Reynolds of about 5,000, and where the turbulent flow is not fully developed, conventional Reynolds Averaged Numerical Simulations (RANS) modelling seems not suitable and either Large Eddy Simulations (LES) or Direct Numerical Simulations (DNS) are preferred (Mittal et al., 2003). In the current numerical investigation, laminar simulations are conducted in the acceleration phase of the pulsatile flow in the ascending region of the aortic arch, with the intension to calibrate the developed sensors. During this ramp-up part, the flow is expected to stay laminar, whereas transition in turbulence is expected later, during the deceleration phase.

The Reynolds number defined by the peak velocity of the pulse is $Re = 5415$, while considering the mean, $U_m = 0.19\ m/s$, it is $Re = 1082$, which indicate that the flow is in a transitional regime. However, for the estimation and the assessment of the resolution of the CFD computations, one may assume that the smallest scales characterizing the flow in a fully developed turbulent regime, can be approximated from the spatial and temporal Kolmogorov scales. These scales are calculated as $\eta_k = (\nu^3/\varepsilon)^{1/4} = 39.6\mu m$ and $\tau_k = \sqrt{\nu/\varepsilon} = 0.36ms$ respectively, assuming the dissipation rate is estimated by the peak velocity as $\varepsilon = U_p^3/D_A = 34.3m^2/s^3$. The same scales, calculated for the mean velocity, with $\varepsilon' = 0.274m^2/s^3$, receive higher values, $\eta_k' = 132\mu m$ and $\tau_k' = 4ms$ respectively.

With regards to those scales, the middle computational mesh, features cells of size of $11 - 14.25 \times \eta_k$ over the wall, and $6.25\eta_k$ in the core of the aorta, in the arch and the branches. Similarly, the coarse and fine mesh have a resolution of $15 - 30 \times \eta_k$ and $8.25 - 10 \times \eta_k$ on the wall respectively, while $10 \times \eta_k$ and $5.25 \times \eta_k$ in the core. Similar resolution levels have been used in computational studies of vascular flows, either in idealised or anatomic models, found in the literature, where structured meshes are employed and the average cell size can be estimated around $3 - 4 \times \eta_k$ (Borazjani et al., 2008; Dasi et al., 2007; De Tullio et al., 2009; Ge et al., 2008). Therefore, the resolution of the fine grid seems able to correctly resolve the features of the flow. The good agreement between the results of the middle grid and the experimental PIV data at peak systole, presented in previous section, as well as the convergence on the predictions of middle and fine grids, strongly suggest that further refinement of the mesh would not alter the results.

Denser grids, would assert that fully resolved DNS computations are performed, however they would require significantly more computational power. As it can be seen from the last column of Table B.2, where the computational cost of the simulation of the entire pulse is given, the computations are demanding and the required resources increase rapidly with the enhancement of the spatial resolution. While the computations on the coarse grid are feasible on a workstation equipped with a multi-thread processor, the fine grid calculations require a multi-processor cluster. It has to be noted that the simulation past the peak systole, is more demanding because of the higher velocities and the more complex flow structures that have been developed. A fully resolved DNS computation on a similar grid with average cell size of $4 \times \eta_k$, would cost more than 2 times what the fine mesh costed, while a model discretised by a homogeneous grid with cell size of η_k, would increase exponentially the cost. On the other hand, while Kolmogorov scales govern the resolution of DNS calculations, the Taylor spatial micro-scale, which can be estimated as $\lambda = \sqrt{10} \cdot Re_{U_p}^{-1/2} \cdot D_A = 1.1mm$, is relevant to LES computations. It can be seen that the size of a mesh accommodating this scale, which is approximately 20 times greater than the equivalent Kolmogorov scale, would be between the size of the coarse and the middle mesh used herein, and the resources needed would be equivalent or higher than those needed for the middle mesh. As a reference, the computational cost of a test simulation of a bileaflet MHV on a 2.5 million cells unstructured tetrahedral mesh, following a similar laminar approach needed 6600 CPUh only up to peak systole, while when employing LES the cost jumped to 7600 CPUh. Thus, for the purposes of in-situ calibration of the WS sensors, the process followed in the current study, which combines the fast and automatic grid generation with laminar numerical simulations, seems more appropriate.